Bio-Design and Manufacturing (2026) 9:335–356
https://doi.org/10.1631/bdm.2500461

RESEARCH ARTICLE

Reconstruction of the macrophage and myelin debris ecosystem following spinal cord injury: a dual-matrix hydrogel/polycaprolactone platform

Tao Xu[1,2] · **Yuchen Zhou**[1] · **Wei Han**[3] · **Xiaohui Ni**[2] · **Mengke Liu**[4] · **Renyue Hu**[5] · **Wei Shi**[1] · **Yahong Zhao**[4] · **Yumin Yang**[1,4] · **Xiaoqing Chen**[1]

Received: 9 September 2025 / Accepted: 25 October 2025 / Published online: 2 March 2026

Abstract

Spinal cord injury (SCI) causes severe trauma to the central nervous system (CNS), involving complex pathological processes such as oxidative stress, inflammation, demyelination, and scar formation. During SCI progression, ongoing myelin degeneration leads to the release of myelin debris, which directly inhibits neural regeneration and impairs functional recovery following the injury. Moreover, bone marrow-derived macrophages (BMDMs) infiltrate the injured site and extensively phagocytose myelin debris, transforming into lipid-laden foam cells. These foam cells accumulate at the lesion core, significantly promoting fibrotic scar formation. To address these challenges, we developed a composite scaffold consisting of a foam cell membrane-coated polycaprolactone (PCL) nanofiber membrane that was integrated with a dual-matrix human acellular amniotic membrane (HAAM) hydrogel. A comprehensive evaluation combining material characterization, in vitro assays, and in vivo assessment using a Sprague–Dawley rat spinal cord defect model demonstrated that the scaffold retains the bioactive properties of HAAM, effectively clearing myelin debris and mitigating foam cell accumulation while concurrently promoting neural regeneration following SCI. The proposed novel biomaterial-based strategy offers a promising approach to addressing the persistent accumulation of myelin debris after SCI.

Tao Xu, Yuchen Zhou, and Wei Han have contributed equally to this work.

✉ Yahong Zhao
zhaoyh108@ntu.edu.cn

✉ Yumin Yang
yangym@ntu.edu.cn

✉ Xiaoqing Chen
chenxiaoqing@ntu.edu.cn

[1] Department of Spine Surgery, Affiliated Hospital of Nantong University, Medical School of Nantong University, Nantong 226001, China

[2] Yancheng Dafeng People's Hospital, Affiliated Hospital of Xinglin College of Nantong University, Yancheng 224115, China

[3] Institute of Regenerative Biology and Medicine, Helmholtz Zentrum München, Munich University, Munich 81377, Germany

[4] Key Laboratory of Neuroregeneration of Jiangsu and Ministry of Education, Co-innovation Center of Neuroregeneration, NMPA Key Laboratory for Research and Evaluation of Tissue Engineering Technology Products, Nantong University, Nantong 226001, China

[5] Department of Endocrinology and Metabolism, Affiliated Hospital of Nantong University, Nantong 226001, China

Graphical abstract

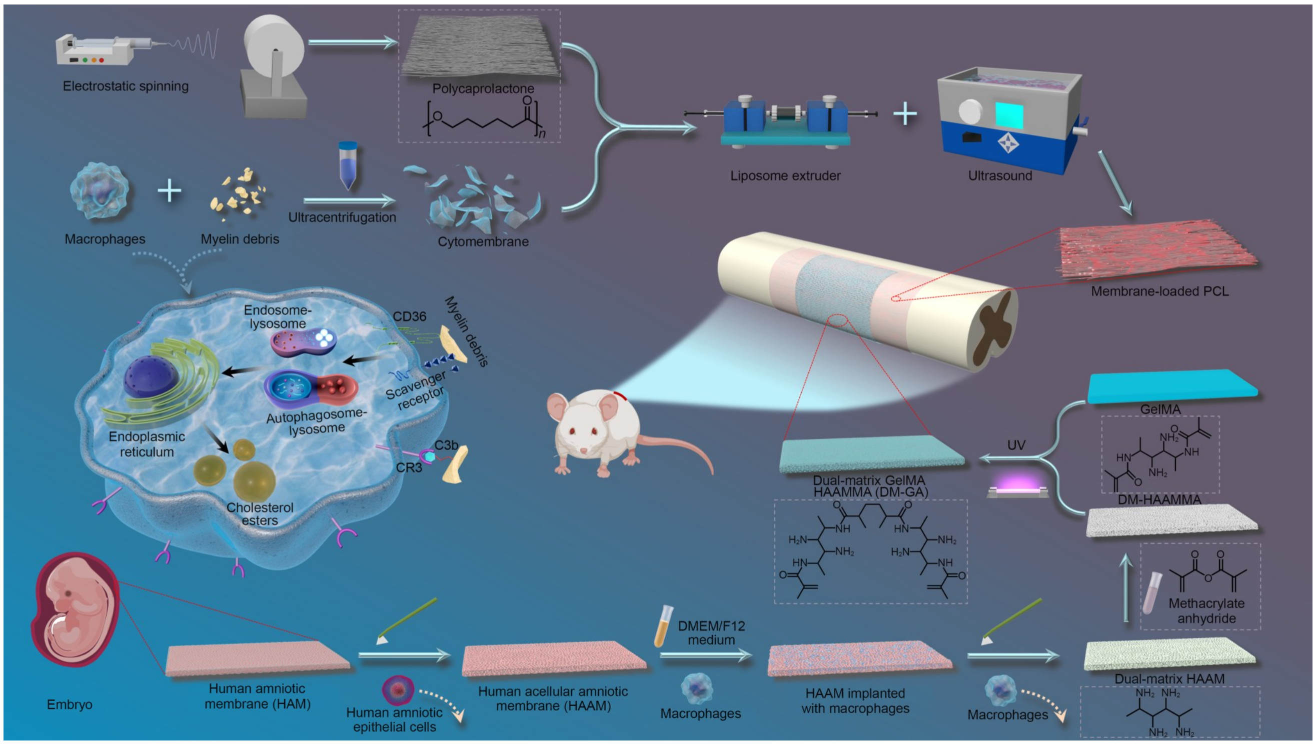

Keywords Spinal cord injury (SCI) · Nerve regeneration · Foam cell · Biomaterials

1 Introduction

Spinal cord injury (SCI) constitutes a severe trauma to the central nervous system (CNS), which often leads to severe motor, sensory, and autonomic dysfunction and can be fatal [1]. SCI encompasses a complex pathological cascade involving oxidative stress, inflammatory responses, demyelination, and scar formation. The disintegration of myelin sheath leads to the continuous release of abundant myelin debris, primarily composed of myelin lipids [2]. This myelin debris contains several proteins that inhibit axonal regeneration, including myelin-associated glycoprotein, Nogo-A, and oligodendrocyte-myelin glycoprotein (OMgp). It can therefore act as a direct inflammatory stimulus [3]. Furthermore, phagocytes, primarily bone marrow-derived macrophages (BMDMs), along with microglia, infiltrate the lesion site extensively after injury [4, 5]. These cells disrupt intracellular lipid homeostasis by phagocytosing myelin debris. Their morphology and pathology closely resemble foam cells observed in atherosclerotic plaques [6]. During the progression of SCI, these foam cells persistently accumulate within the lesion, forming a primary component of fibrotic scar tissue that impedes axonal passage [7].

Current therapeutic strategies target the following three activities of BMDMs: reducing the uptake of myelin debris [8, 9], enhancing their lipophagic capacity [10, 11], and promoting intracellular lipid efflux [12]. These methods focus on regulating phagocyte activity at RNA and protein levels, partially mitigating foam cell accumulation. However, this strategy presents inherent limitations. Specifically, myelin debris generated after SCI exerts dual negative effects on axonal regeneration. The direct impact stems from its neurotoxicity, which triggers the phagocytic activity of BMDMs to prevent immediate impairment of neural repair. Indirectly, myelin debris-phagocytosing BMDMs develop intracellular lipid overload, transforming into foam cells that exacerbate fibrotic scarring [13]. However, addressing both these effects of myelin debris remains a major challenge. In our previous work [14], we engineered nanoscaffolds capable of modulating lipid metabolism in contused spinal cord environments, conducted a comprehensive analysis of myelin debris and foam cells, and identified significant potential for biomaterial-based approaches.

Compared to gene editing or protein modulation, biomaterials offer diversified structures and compositions that exert direct, broad-spectrum effects at lesion sites [15].

Moreover, pro-angiogenic biomaterials can supply sufficient metabolic energy to accelerate tissue recovery [16]. In our preceding studies [17–19], we integrated human acellular amniotic membrane (HAAM) to fabricate composite hydrogels that effectively promote post-SCI neovascularization, providing structural and metabolic support for axonal regeneration and cellular activities at spinal cord stumps.

In this work, we fabricated a composite scaffold (dual matrix/gelatin methacryloyl (GelMA)–HAAMMA/membrane-loaded polycaprolactone (DM-GA-MLPCL)), integrating foamy macrophage membrane-coated polycaprolactone (MM-PCL) nanofibers with a dual-matrix HAAM hydrogel, aimed at treating severe spinal cord defects. Initially, by determining the molecular weight and concentration of PCL, we fabricated an axially aligned PCL fiber membrane via electrospinning. To enhance the scaffold's functional properties, we developed a foam cell MM-PCL. In vitro and in vivo experiments demonstrated that MM-PCL can efficiently adsorb myelin debris and induce BMDM migration toward myelin debris-loaded nanofiber membranes. This mechanism effectively prevents foam cell accumulation in the lesion core, facilitating SCI recovery. Subsequently, macrophages were seeded onto an HAAM that had undergone multiple rounds of decellularization, yielding a dual-matrix (DM)-HAAM. Following methylation-based chemical grafting modification, a photocrosslinkable DM-HAAM-based hydrogel (DM-GA) was successfully prepared. The three-dimensional (3D) distribution of co-cultured macrophages was examined using confocal microscopy and cellular assays, which confirmed that DM-GA accelerates macrophage migration toward areas containing myelin debris while effectively preventing foam cell deposition within the lesion. In vivo studies involving a spinal cord defect model revealed that DM-GA-MLPCL successfully translocated myelin debris from the lesion core, prevented foam cell deposition, and facilitated the passage of regenerating axons.

Furthermore, multi-omics analysis confirmed that the composite scaffold effectively regulates lipid metabolism at the SCI site following adsorption of myelin debris. The study also identified significant metabolic similarities between SCI-associated foam cells and those observed in other pathologies, offering new insights for designing biomaterials that could be combined with gene-editing therapies for SCI.

2 Results

2.1 Preparation and characterization of HAAM, DM-HAAM, and DM-HAAMMA

The native human amniotic membrane (HAM) isolated from surgical waste appeared as a thin, pink-colored biological film (Fig. 1a). This HAM was then subjected to decellularization and subsequently placed in ultra-pure water, represented by the transparent membrane (Fig. 1b). Scanning electron microscopy (SEM) analysis revealed the matrix and fibrous surfaces of HAAM, as depicted in Figs. 1c and 1d, respectively, with no detectable cellular debris. The hematoxylin and eosin (H&E)-stained sections showed a lack of nuclei in HAAM [20, 21], whereas native HAM clearly showed neatly arranged cells (Figs. 1e and 1f) (n=3). These findings confirmed that HAM had been successfully decellularized into HAAM, as confirmed by gross observation, SEM, and H&E staining.

Using a meticulous seeding procedure, macrophages were successfully cultured on the HAAM surface. SEM imaging revealed a substantial number of adhered and proliferating macrophages on the HAAM surface (Fig. 1h). In the magnified view shown in Fig. 1k, the characteristic pseudopodia, indicative of macrophage proliferation, are clearly visible [22, 23]. Similarly, to confirm the presence of a bilayer extracellular matrix (ECM), cultured macrophages were analyzed by SEM after decellularization. The surfaces of decellularized HAAMs were uniformly and abundantly enriched with macrophage-derived ECM (Fig. 1i). Collectively, these findings confirm the successful preparation of DM-HAAM.

SEM validation of DM-HAAMMA showed that the matrix structure remained intact after grafting (Fig. 1g). Consistent with our previous research [19], the Fourier transform infrared spectroscopy (FTIR) analysis results confirm the effectiveness of methacrylic anhydride (MA) grafting (Fig. 1r). As shown in the figure, the backbone structures of DM-HAAM and DM-HAAMMA are similar. The normal amide A band of DM-HAAM is centered at 3293 cm^{-1}, primarily attributed to N–H vibrational contraction, while DM-HAAMMA acrylamide appears at the same peak, exhibiting higher absorbance, consistent with successful grafting. These findings confirm the successful grafting of MA onto DM-HAAM.

2.2 Synthesis and characterization of DM-GA

After synthesizing DM-GA, we analyzed its morphology using SEM (Fig. 1j) and subsequently compared its average pore size distribution with that of GA (Figs. 1m and 1n). The results indicate that DM-GA featured a loose, porous structure that supported the activity and migration of macrophages and neural stem cells. Specifically, the average pore size of DM-GA was measured at (55.07±11.34) μm, which closely resembled that of natural ECM rather than GA ((22.19±8.80) μm) [24]. This characteristic ensures ample space for neural cells and macrophages to extend pseudopodia and migrate across pores, thereby promoting cell infiltration within the 3D network. In contrast, hydrogels with smaller pore sizes may hinder cytoskeletal reorganization,

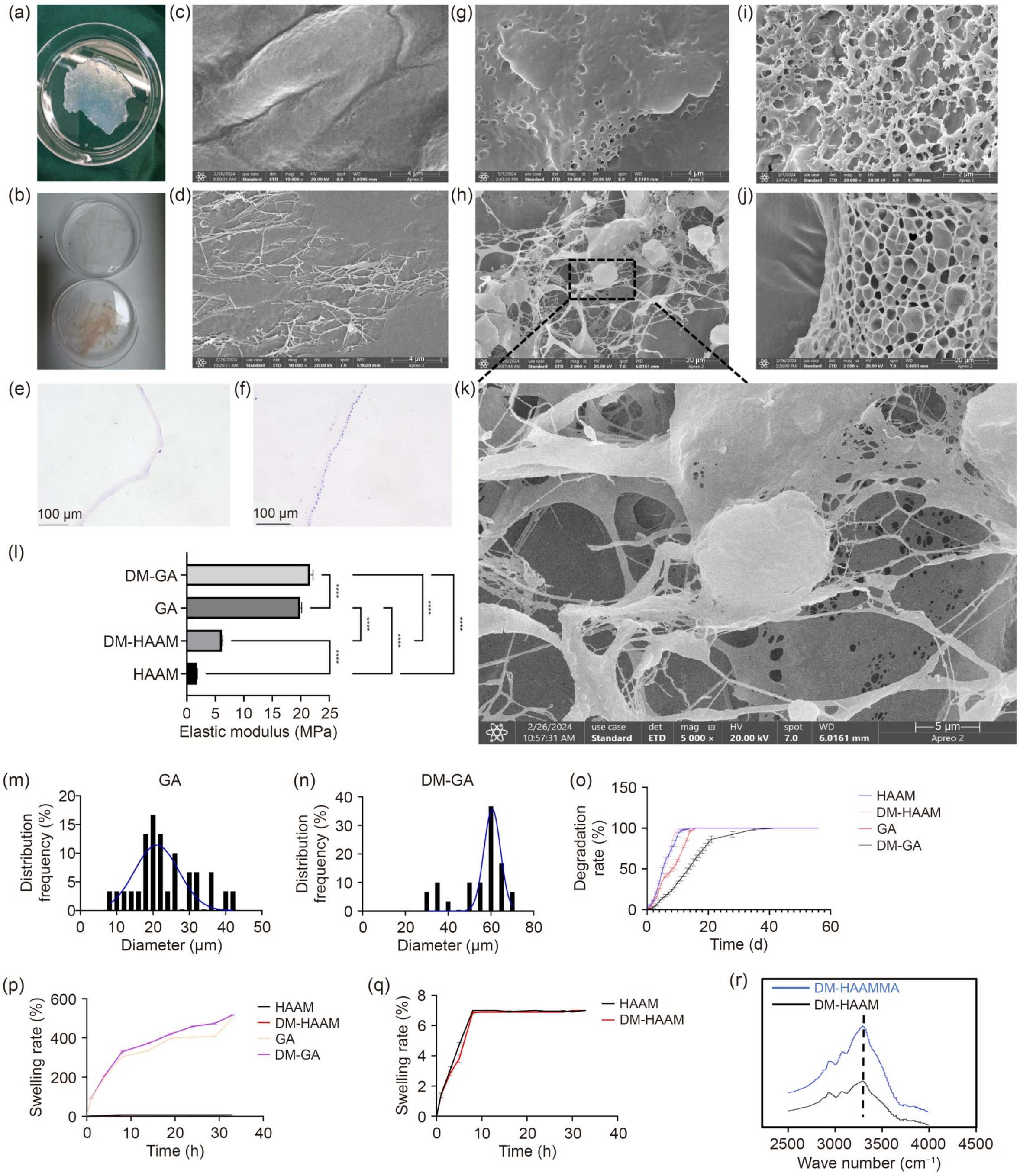

Fig. 1 Synthesis and characterization of HAAM, DM-HAAM, GA, and DM-GA. (a) Actual HAM sample obtained from surgical waste. (b) Actual shots of HAAM (top) and HAM (bottom). Representative SEM images of the substrate (c) and fiber (d) sides of HAAM; scale bars: 4 μm (10,000×). H&E staining images of HAAM (e) and HAM (f); scale bars: 100 μm (20×). (g) Representative SEM image of DM-HAAMMA; scale bar: 4 μm (10,000×). SEM images of HAAM after incubation with Raw264.7 cells (h), DM-HAAM without Raw264.7 cells (i), and DM-GA (j); scale bars: 20 μm (2000×) for (h, j) and 2 μm (20,000×) for (i). (k) Local magnification of (h). (l) Elastic modulus of HAAM, DM-HAAM, GA, and DM-GA (n=3). Mean pore size distributions of GA (m) and DM-GA (n) (both n=3). (o) Degradation rates of HAAM, DM-HAAM, GA, and DM-GA (n=5). (p) Swelling rates of HAAM, DM-HAAM, GA, and DM-GA (n=5). (q) Swelling rates of HAAM and DM-HAAM (n= 5). (r) Comparative analysis of FTIR spectra for DM-HAAM and DM-HAAMMA. Data in (l, o–q) are expressed as mean±standard deviation. $^{****}p<0.0001$

restricting cell migration to mere surface adhesion. According to Fick's law, larger pores enhance the diffusion of nutrients (e.g., glucose and oxygen) and metabolic byproducts (e.g., lactic acid and CO_2), particularly in hydrogel scaffolds exceeding 2 mm in thickness [25], thereby preventing central necrosis. Furthermore, the pore size of DM-GA closely matches the initial invasion scale of capillary buds during angiogenesis (50–100 μm), enabling human umbilical vein endothelial cells (HUVECs) to form lumen networks more efficiently through these pores [26, 27]. Therefore, DM-GA is ideal for promoting deep cell infiltration, rapid vascularization, and optimal mechanical adaptation within the SCI region.

In the elastic modulus test (Fig. 1l), the values for HAAM, DM-HAAM, GA, and DM-GA were (1.786±0.056), (6.166±0.116), (19.814±0.290), and (21.616±0.612) MPa, respectively. In SCI defect models, the injured ends continuously undergo varying degrees of deformation due to back activity. However, hydrogels with a high elastic modulus can provide sufficient rigidity to resist local compression and shear stress following SCI, thereby preventing cavity formation or secondary injury expansion [28]. The significantly higher elastic modulus of DM-GA compared to the other groups allows it to stabilize the injury site effectively.

The degradation time and swelling coefficient of DM-GA were significantly higher than those of other groups (Figs. 1o–1q). Specifically, the degradation time of DM-GA was extended to (36±1) d, which is notably longer than that of the other groups. This duration fully encompasses the acute and subacute phases following SCI, ensuring sustained release of various bioactive factors from HAAM. Additionally, this timeframe ensures the continuous breakdown and release of myelin debris and macrophage migration [29], thereby enabling DM-GA to interact more effectively with MM-PCL. Besides, DM-GA, with a high swelling ratio of (512.72±6.85)%, can fill irregular cavities caused by SCI through water absorption and expansion. This process facilitates the formation of a tight interface with surrounding tissues, thereby reducing immune cell infiltration and curtailing the spread of inflammation [19].

2.3 Characterization of PCL nanofibrous membranes

Figure 2 illustrates the screening process used to identify the optimal electrospinning conditions for the mainstream PCL electrospinning method. PCL with four different molecular weights (4.5W, 6W, 8W, and 10W) was dissolved in hexafluoroisopropanol at varying concentrations (6%, 8%, 10%, and 12%, i.e., 0.06, 0.08, 0.10, and 0.12 g/mL). The SEM morphologies of PCL-oriented nanofiber membranes prepared under 16 different conditions are detailed in Fig. 2a. Subsequently, the most suitable PCL molecular weight was identified using effective oriented fiber statistics (Fig. 2b), which revealed that the 8W PCL membrane exhibits the highest and most stable number of effectively oriented fibers. The proportions of effectively oriented fibers at different PCL dissolution concentrations were as follows: (87.4±1.14)% (6% concentration), (88.8±1.09)% (8% concentration), (91.6±1.51)% (10% concentration), and (86±1.41)% (12% concentration). The average diameter distribution of PCL nanofiber membranes at the four dissolved concentrations was calculated to assess their biological properties. As shown in Figs. 2c–2f, the average diameters of PCL nanofibers at dissolved concentrations of 6%, 8%, 10%, and 12% were (664.266±191.916), (698.366±184.908), (734.733±68.653), and (813.900±116.148) nm, respectively. The PCL nanofiber membrane with a molecular weight of 8W and a dissolution concentration of 10% exhibited the greatest number of effectively oriented fibers and the most stable diameter distribution. Its fiber diameter of approximately 700 nm is ideal for promoting macrophage and endothelial cell infiltration, angiogenesis, and ECM deposition, thereby forming a 3D microenvironment conducive to nerve regeneration [30–32]. In summary, we prepared PCL nanofiber membranes using 8W PCL dissolved in 10% hexafluoroisopropanol.

2.4 Validation of foam cells and extraction of cell membranes

Foam cells were generated through the co-culture of spinal cord homogenate and Raw264.7 macrophages. Figure 3a presents the light microscopic image of Raw264.7 cells under normal conditions. After engulfing myelin debris, the volume of Raw264.7 cells significantly increased, and a substantial number of red particles (cholesteryl esters) appeared within the cells (Oil Red O (ORO) staining) (Fig. 3b). This indicates that the macrophages had successfully transformed into foam cells.

Figures 3g and 3h present the transmission electron microscopy (TEM) morphologies of Raw264.7 and foam cells, respectively. Compared with macrophages under normal conditions, the cytoplasm of foam cells contained a significant number of yellowish cholesterol lipid droplets (marked by yellow circles). The TEM results of foam cells align with the cell morphology observed under light microscopy. This confirmed that the foam cells are the source of the subsequent cell membrane extraction.

TEM analysis of the extracted cell membrane clearly demonstrated that macrophage organelles were successfully removed via differential centrifugation, leaving only the lipid bilayer of the cell membrane (Fig. 3e). CD36 antibody immunofluorescence (IF) staining was used to quantify the receptor density on the cell membranes of macrophages and foam cells (Fig. 3k). As shown in the corresponding quantitative statistics in Fig. 3i, the CD36 IF density for foam cells was 3752±102, significantly higher than that of ordinary macrophages (1298±79). These findings validate the rationale and effectiveness of using the foam cell membrane extraction method to enhance its capacity for adsorbing myelin debris.

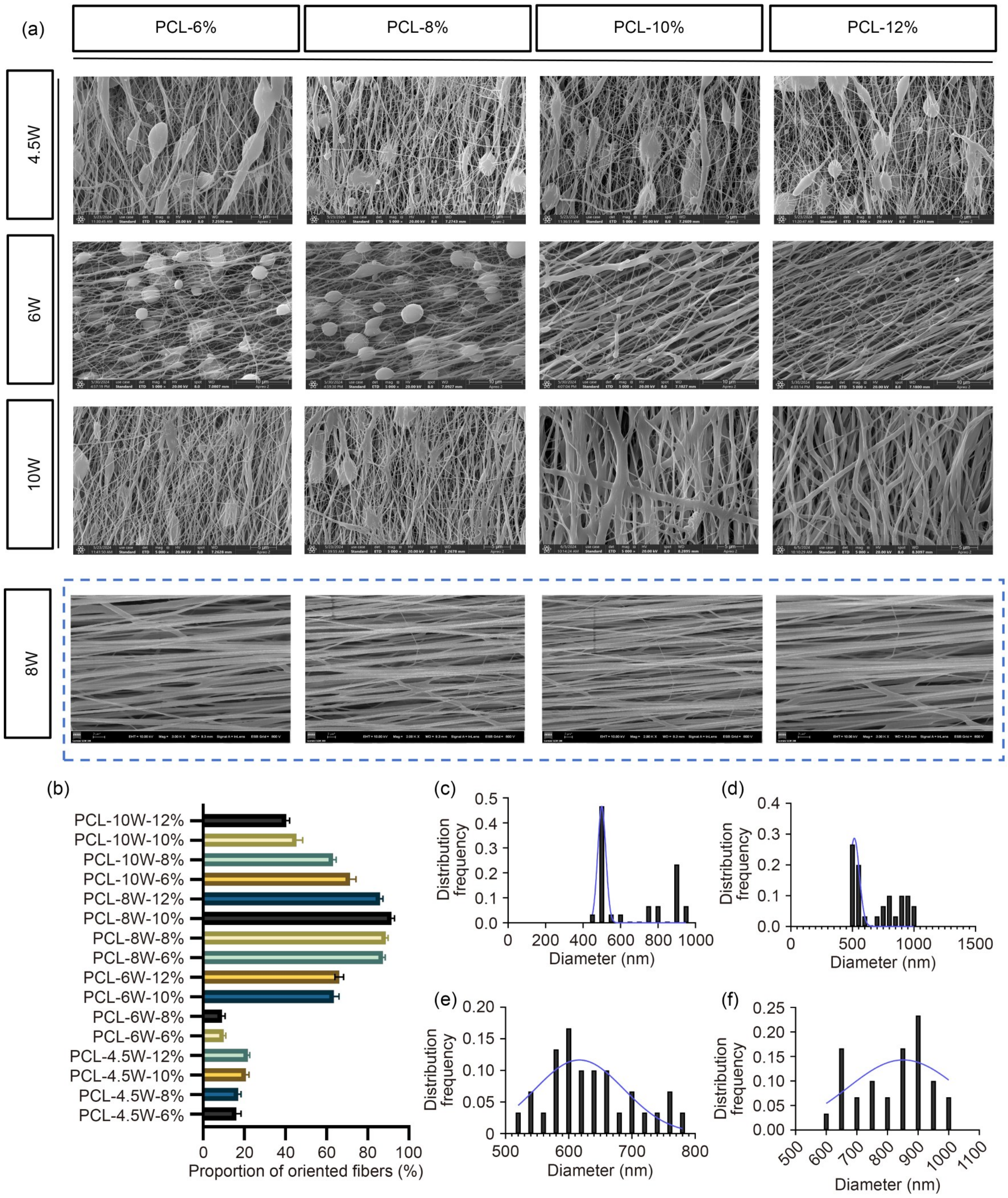

Fig. 2 Preparation and screening of PCL nanofibrous membranes (*n*=5). (a) SEM images of PCL-oriented nanofiber membranes with different molecular weights and dissolved concentrations; scale bars: 5 μm for the first and third rows, 10 μm for the second row (5000×), and 2 μm for the fourth row. (b) The proportion of limited axial fiber number for PCL axial nanofiber membranes under 16 different preparation conditions. Distribution of the mean fiber diameters of PCL-8W-6% (c), PCL-8W-8% (d), PCL-8W-10% (e), and PCL-8W-12% (f). Data in (b) are expressed as mean±standard deviation

Co-localization of myelin basic protein (MBP) and CD36 was investigated to determine whether the enhanced ability of foam cell membranes to bind myelin debris could be attributed to an increased number of surface receptors, as indicated in our IF co-localization results (Figs. 3l and 3j). The data indicated that adsorbed myelin debris (MBP) and surface receptors (CD36) co-localized almost completely in normal macrophages and foam cells. These findings confirm that foam cell membranes indeed exhibit a greater capacity to absorb myelin debris, most likely due to the increased density of membrane surface receptors.

We also evaluated the upper limit of myelin debris adsorbed per unit area of the foam cells' membrane to ensure that the coated cell membrane could continuously absorb myelin debris generated in the corresponding region without reaching saturation. For further details, please refer to Supplementary Material 5 in the supplementary information.

2.5 Characterization of MM-PCL

Figures 3c and 3d illustrate the fabrication of MM-PCL using a liposome extruder coupled with ultrasonic vibration. Atomic force microscope (AFM)-based heat maps (Fig. 3o) revealed that the surface morphology of MM-PCL was substantially altered compared to native PCL, attributable to the cell membrane coating. SEM topography revealed that the underlying aligned PCL nanofiber structure was effectively covered by the foam cell membrane (Fig. 3f). FTIR spectroscopy (Fig. 3m) results verified the successful coating of the foam cell membrane onto PCL (*n*=5). The FTIR spectrum of MM-PCL showed a broad peak at 3200–3600 cm^{-1}, characteristic of MM and absent in PCL, attributed to hydroxyl groups in the membrane glycocalyx and suggesting enhanced hydrophilicity. Furthermore, in the C–H stretching region (2850–2950 cm^{-1}), signals from phospholipid alkyl chains in the MM overlapped with the methylene peaks of PCL. These findings, along with the X-ray photoelectron spectroscopy (XPS) analysis results (Figs. 3n and

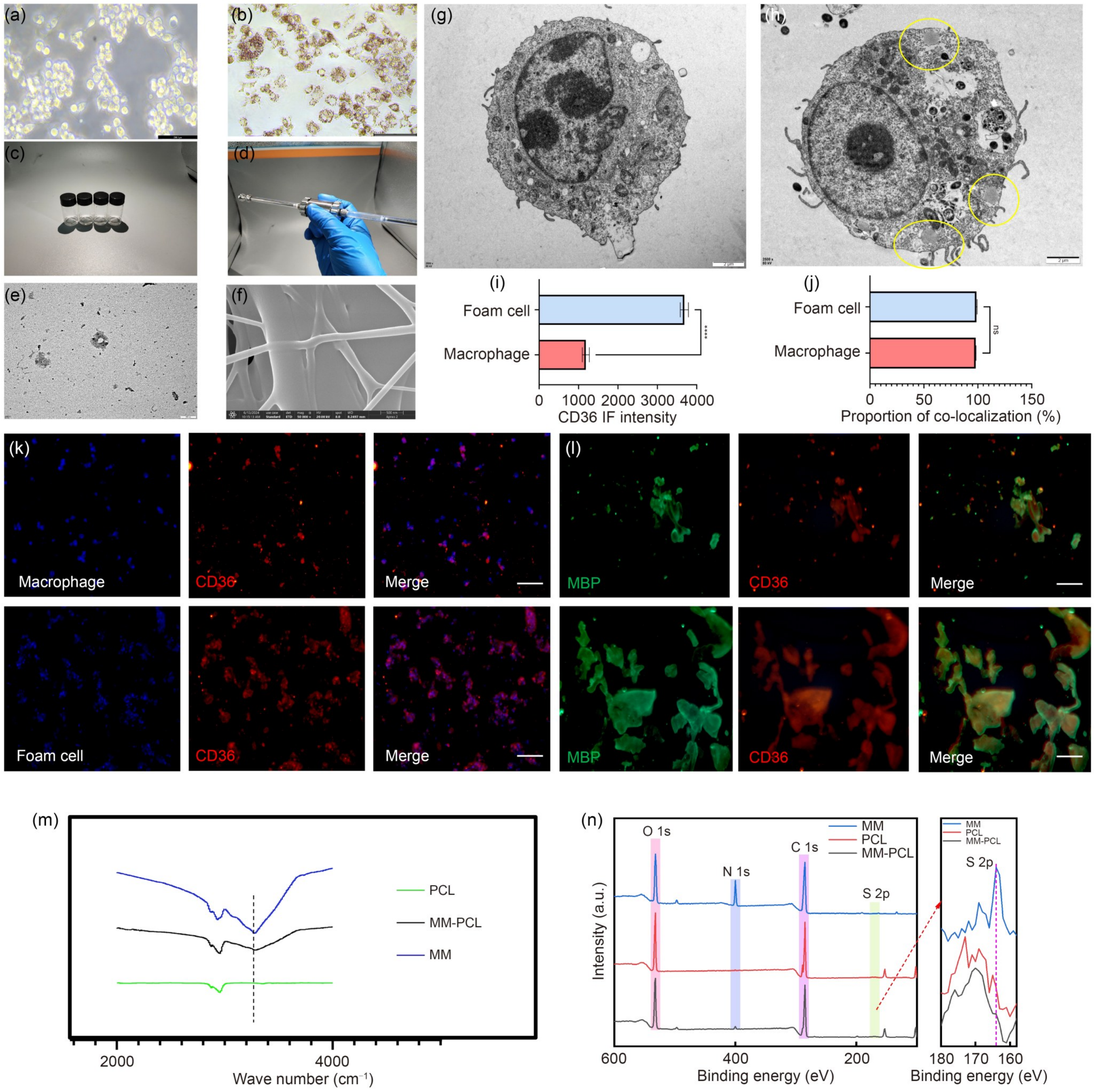

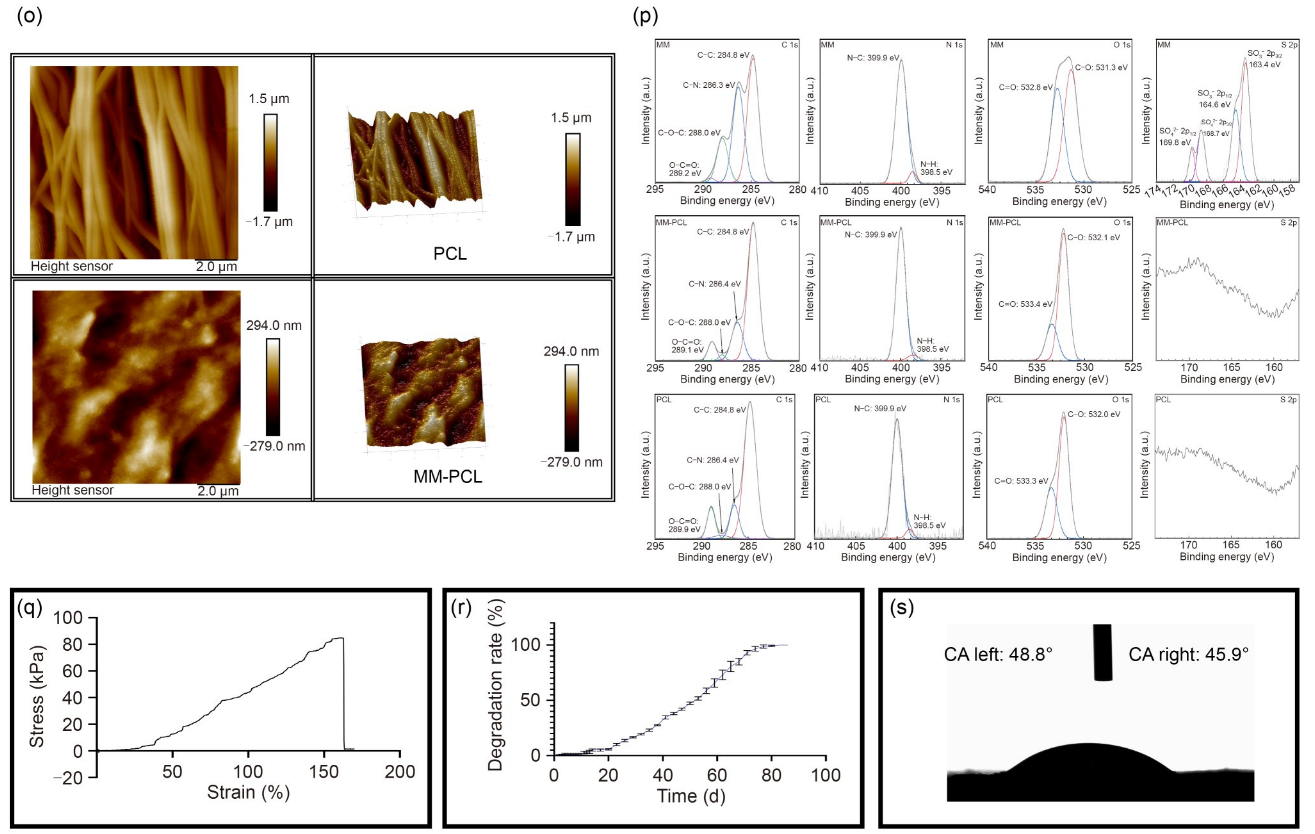

Fig. 3 Extraction of foamy macrophage membranes and characterization of DM-GA. ORO staining images of Raw264.7 (a) and foam (b) cells; scale bars: 200 µm (20×). (c, d) Actual beating maps of MM-PCL prepared using ultrasonic vibration and liposome extrusion methods in an ice chamber. (e) Extracted TEM image of the cell membrane; scale bar: 50 µm (20×). (f) SEM image of MM-PCL; scale bar: 500 nm (50,000×). TEM images of Raw264.7 cells in physiological state (g) and foam cells (h); scale bars: 2 µm (2000×). (i) CD36 fluorescence intensity statistics for macrophages and foam cells (*n*=5). (j) Co-localization coincidence rate statistics for CD36 receptor and MBP-labeled myelin fragments (*n*= 5). (k) CD36 IF staining images of macrophages and foam cells; scale bars: 200 µm (20×). (l) Co-localization fluorescence staining images of MBP-labeled myelin fragments and CD36-labeled membrane receptors; scale bars: 200 µm (20×). FTIR spectral (m) and XPS full-spectra (n) of PCL, MM, and MM-PCL. (o) Atomic force microscopy scanning and heat map of PCL and MM-PCL. (p) XPS elemental analyses (C, N, O, and S) of PCL, MM, and MM-PCL. (q) Stress–strain curve of MM-PCL. (r) Degradation rate of MM-PCL. (s) Water contact angle (CA) of MM-PCL. Data in (i, j, r) are expressed as mean±standard deviation. ns: no significance; $^{****}p<0.0001$. For detailed physicochemical properties of PCL, please refer to the official website of Chemistry

3p), collectively confirm that the foam cell membrane coating was successfully applied to the PCL nanofibers [30]. While the PCL substrate showed negligible nitrogen (N) and sulfur (S) signals (a weak S signal arose from processing additives), distinct N and S signals, indicative of membrane proteins and glycosaminoglycans from the MM, were detected on MM-PCL. The marked increase in N content provided strong evidence for the effectiveness of the cell membrane coating [32–34].

Mechanical testing revealed that MM-PCL exhibited an ultimate strain of 162%, indicating adequate flexibility to cover the SCI site [35] (Fig. 3q). The degradation profile showed a complete degradation time of (79±1) d (Fig. 3r), which spans the inflammatory (1–2 weeks), proliferation (2–6 weeks), and remodeling (lasting for months) phases post-SCI. This timeline also ensures that MM-PCL can persistently absorb myelin debris throughout its release period [36]. Water contact angle measurements (Fig. 3s) demonstrated that the MM coating significantly enhanced the hydrophilicity of the otherwise hydrophobic PCL (contact angle approximately 70°–100° [37, 38]), reducing the average contact angle of MM-PCL to 47.3°±2.05°. This increased hydrophilicity favors cell infiltration and matrix deposition [34, 39]. Detailed adhesion data for MM-PCL are provided in Supplementary Material 5 (supplementary information).

2.6 DM-GA enhances macrophage migration

Confocal 3D heat maps showing macrophage distribution after 24 and 72 h of co-culture showed that the macrophages in the DM-GA group accumulated more densely around myelin debris than those in the GA group (Fig. 4a). These results underscore the importance of the dual-ECM modification in GA. DM-GA-MLPCL enhances the recruitment

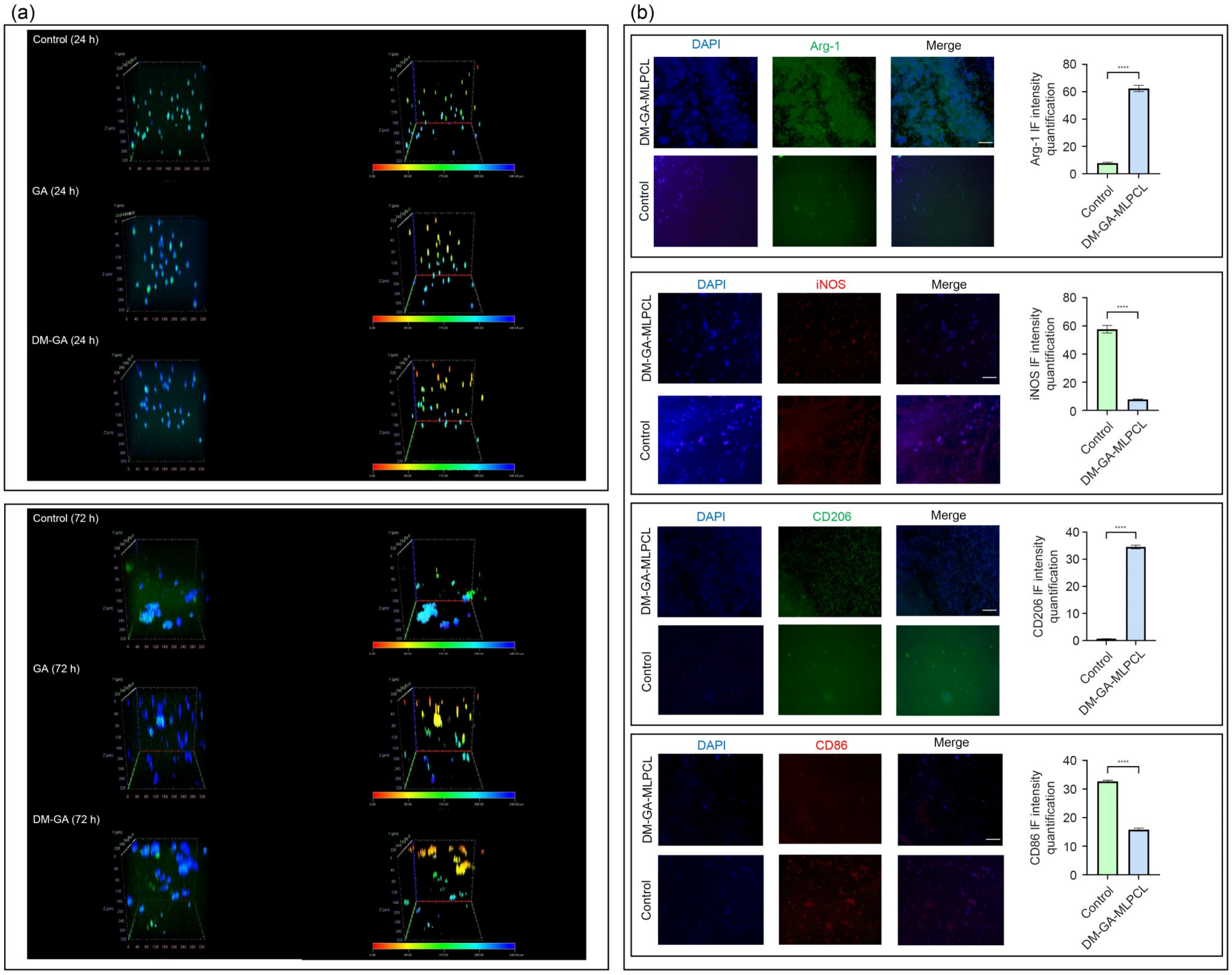

Fig. 4 The collaborative ability among the components of DM-GA-MLPCL. (a) Heat maps (2000×) representing the results of confocal 3D analysis of macrophage migration in co-culture at 24 and 72 h for the control, GA, and DM-GA groups. The *X*, *Y*, and *Z* axes represent cell density, migration distance, and culture interface width, respectively. (b) IF staining images of Arg-1, iNOS, CD206, and CD86 in the culture environments of the DM-GA-MLPCL and control groups. Scale bars: 200 μm (20×). Data in (b) are expressed as mean±standard deviation (n=5). $^{****}p<0.0001$. DAPI: 4′,6-diamidino-2′-phenylindole

of BMDMs to the myelin debris site, facilitating its clearance while preventing excessive accumulation of BMDMs in the lesion core, thereby reducing scar formation [40].

2.7 DM-GA-MLPCL modulates macrophage phenotype

We next investigated whether DM-GA-MLPCL affects the macrophage phenotype to improve the post-SCI immune microenvironment. While foam cell phenotypes have not been precisely defined in the context of SCI [40], this study focused on the transition from pro-inflammatory (M1-like) to anti-inflammatory (M2-like) states to assess the therapeutic potential of the composite, rather than defining the foam cell phenotype. Macrophage polarization was assessed via IF following co-culture with myelin debris and DM-GA-MLPCL (Fig. 4b). Quantitative analysis showed a significant increase in the IF intensity of M2 markers Arg-1 (DM-GA-MLPCL: 64.69±3.09 vs. control: 8.36±1.92) and CD206 (DM-GA-MLPCL: 33.91±2.12 vs. control: 0.41±0.07). Conversely, the IF intensity of M1 markers inducible nitric oxide synthase (iNOS) (DM-GA-MLPCL: 7.04±0.08 vs. control: 57.12±4.09) and CD86 (DM-GA-MLPCL: 16.85±2.03 vs. control: 33.56±2.27) was markedly reduced. These results indicate that DM-GA-MLPCL promotes a shift toward an M2-dominant, anti-inflammatory phenotype, contrasting with the typical M1-dominant environment in the injured spinal cord. This suggests that DM-GA-MLPCL can remodel the local immune cell repertoire by suppressing pro-inflammatory subsets and fostering an overall homeostatic microenvironment [6]. Minor blurring in some IF images is noted, which might be due to the inherent fluorescence from PCL and myelin debris.

Consistent with these findings, IF analysis of macrophages adherent to the DM-GA-MLPCL scaffold itself (Fig. 5a) revealed a predominance of iNOS$^+$ and CD86$^+$ cells (M1-like). This phenotype aligns with that of the foam cells characterized earlier and supports the notion that DM-GA-MLPCL facilitates their migration away from the injury core. Schematics of the 3D co-culture and Transwell experimental setups are shown in Figs. 5b and 5c, respectively.

2.8 DM-GA-MLPCL retains the biological efficacy of GA

Ideally, the components of a composite biomaterial should act synergistically without compromising each other's bioactivity. We therefore assessed whether the composite scaffold (DM-GA-MLPCL) retained the bioactivity of its DM-GA component by performing HUVEC migration, invasion, and angiogenesis assays. Additionally, a Raw264.7 macrophage invasion assay was conducted to ensure that the adsorption of myelin debris by MM-PCL did not hinder macrophage mobility within the composite.

In the HUVEC migration assay (Figs. 5d and 5h), the migration ratio was significantly enhanced in the DM-GA ((63.91±1.52)%) and DM-GA-MLPCL ((64.02±2.25)%) groups compared to the GA ((50.98±1.52)%), PCL ((30.49±0.23)%), and control ((36.08±0.88)%) groups (n=5, p<0.0001). Similarly, the HUVEC invasion assay (Figs. 5f and 5j) results showed that the DM-GA-MLPCL group exhibited the highest invasion ((84.46±0.73)%), followed by the DM-GA group ((76.59±2.01)%). Both were significantly higher than the GA ((38.79±0.88)%), control ((27.95±1.36)%), and PCL ((1.75±0.51)%) groups. In the tube formation assay (Figs. 5e and 5i), the number of vascular

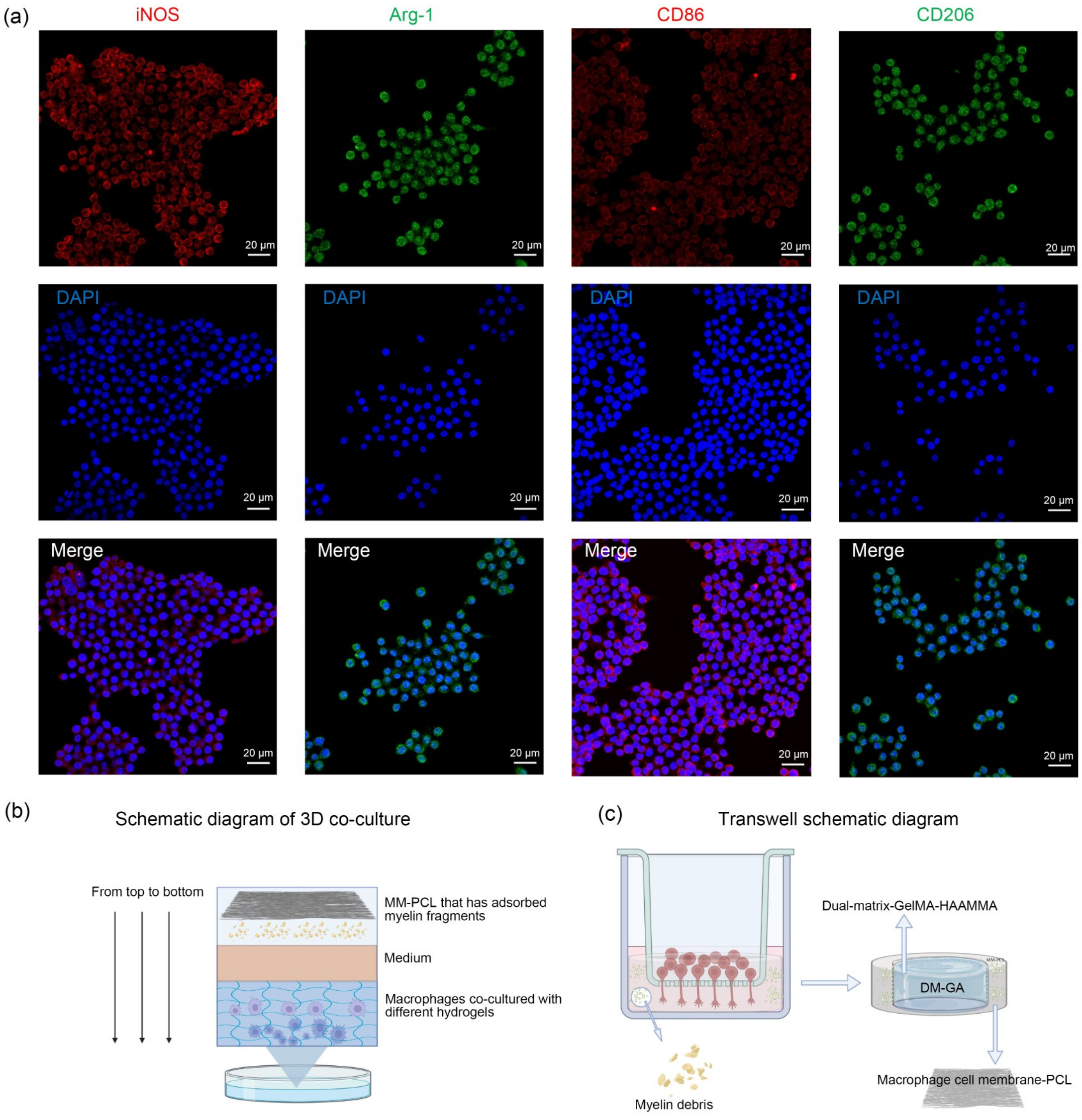

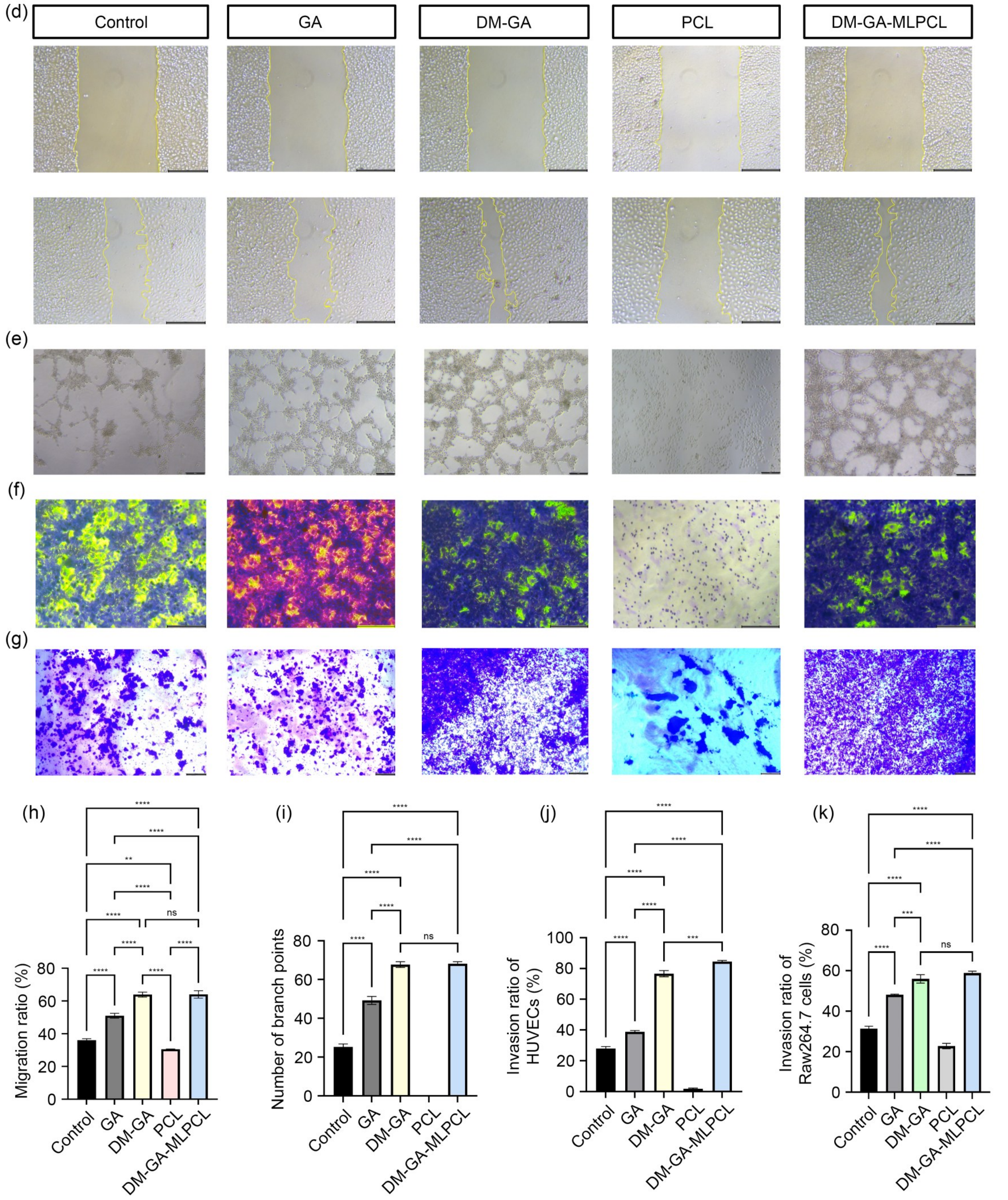

Fig. 5 In vitro cell experiments of DM-GA-MLPCL. (a) IF staining images of iNOS, Arg-1, CD86, and CD206 in macrophages adsorbed onto DM-GA-MLPCL. Scale bars: 20 μm (20×). Schematic illustrations of the 3D co-culture system (b) and Transwell assay (c). (d) Cell migration assay of HUVECs: in vitro cell experiment results showing the control, GA, DM-GA, PCL, and DM-GA-MLPCL groups; scale bars: 200 μm (5×). (e) Tube formation assay of HUVECs; scale bars: 100 μm (5×). Transwell assay results for HUVECs (f, negative color treatment) and Raw264.7 cells (g, normal color); scale bars: 200 μm (5×). (h) Migration ratio of HUVECs (*n*=5). (i) Number of vascular branches formed (*n*= 5). Invasion ratios of HUVECs (j, *n*=5) and Raw264.7 cells (k, *n*=5). Data in (h–k) are expressed as mean±standard deviation. ns: no significance; $^{**}p<0.01$, $^{***}p<0.001$, and $^{****}p<0.0001$

branches was markedly increased in the DM-GA (67.75± 1.52) and DM-GA-MLPCL (68.25±0.95) groups compared to the GA (49.25±2.06), control (25.25±1.50), and PCL (0) groups. These results demonstrate that the pro-angiogenic capacity of DM-GA, conferred by its bilayer ECM, is superior to that of conventional GA. PCL alone lacked any pro-angiogenic effect, underscoring the contribution of the HAAM component. Critically, the bioactivity of DM-GA was fully retained in the final DM-GA-MLPCL composite, as no significant differences were detected between these two groups in the verification related to the angiogenesis ability.

Similarly, in the Raw264.7 macrophage invasion assay (Figs. 5g and 5k), the invasion ratio was highest in the DM-GA-MLPCL ((58.84±0.92)%) and DM-GA ((55.93±2.09)%) groups, which were significantly greater than the GA ((48.12±0.28)%), control ((31.38±1.17)%), and PCL ((22.74±1.34)%) groups. No significant difference was found between the DM-GA-MLPCL and DM-GA groups, indicating that incorporating MM-PCL did not impede macrophage migration.

2.9 Histological assessment of SCI models

Histological evaluation of spinal cord tissue sections stained with Masson and ORO was performed to assess repair outcomes. The MM-PCL group was included to evaluate the consequences of omitting the bioactive DM-GA hydrogel.

Masson's trichrome staining (Fig. 6a) revealed extensive collagen deposition and fibrotic scarring at the injury site in the SCI group. Implantation of MM-PCL alone, without the DM-GA hydrogel filler, resulted in a large cavity at the lesion site, likely due to mechanical instability and disrupted tissue continuity. Contrastingly, the DM-GA and DM-GA-MLPCL groups showed substantially reduced collagen scarring. Quantitative analysis (Fig. 7a) confirmed a significantly lower collagen area percentage in the DM-GA ((25.32±0.93)%) and DM-GA-MLPCL ((21.96±0.63)%) groups compared to the SCI group ((48.31±0.72)%). In comparison, the sham group showed no collagen deposition ((18.74±0.31)%). The cavitated MM-PCL group was excluded from this analysis (*n*=5). ORO staining (Fig. 6b) revealed substantial neutral lipid deposits (red) in the SCI and DM-GA groups. The area of ORO staining was significantly reduced in the MM-PCL ((8.77±0.90)%) and DM-GA-MLPCL ((7.28±0.48)%) groups compared to the SCI ((21.02±1.52)%) and DM-GA ((19.92±1.15)%) groups (Fig. 7a; sham: 0%).

These histological findings highlight the essential and complementary roles of both components in the DM-GA-MLPCL composite. The DM-GA hydrogel provides structural support, fills the lesion cavity, and inhibits fibrotic scarring. At the same time, the MM-PCL membrane ensures adequate clearance of myelin debris and reduces neutral lipid accumulation.

2.10 Neuronal and axonal regeneration

Neurological recovery was assessed by evaluating key neuropathological markers: β3-tubulin (TUBB3), neurofilament 200 (NF200), microtubule-associated protein 2 (MAP2), and glial fibrillary acidic protein (GFAP) [41]. TUBB3 is highly expressed in neuronal cell bodies and axons, serving as a marker for newly formed or regenerated neurons (e.g., neurons differentiated from neural stem cells). An increase in TUBB3 expression indicates active neurogenesis or enhanced survival of mature neurons. NF200 is a marker for the neurofilament skeleton of myelinated axons, reflecting axonal integrity and regeneration (e.g., growth cone formation). Continuous NF200 expression typically signifies an axon traversing the injured region. The distribution of MAP2, which specifically marks dendrites, reflects synaptic remodeling (e.g., dendritic spine density and branching complexity). Enhanced MAP2 signaling suggests dendritic regeneration and potentially the concurrent reconstruction of neuronal networks. The distribution of GFAP, a marker of activated astrocytes, correlates with scar compactness. GFAP-positive areas represent regions of glial scarring.

IF analysis (Figs. 7a and 8) demonstrated superior neural repair in the DM-GA-MLPCL group compared to all other groups. The fluorescence intensity of TUBB3, indicative of neuronal regeneration/survival, was markedly higher in the DM-GA-MLPCL group (178.40±5.02) than in the SCI (26.00±2.12) and MM-PCL (18.80±1.48) groups, and was comparable to the DM-GA group (175.20±1.48; $p>0.05$). Similarly, the IF intensity of MAP2 (dendritic remodeling) was significantly higher in the DM-GA-MLPCL group (129.60±3.71) than in the SCI (43.20±5.63), DM-GA (120.40±1.14), and MM-PCL (67.80±5.63) groups. Similarly, the NF200 intensity (axonal regeneration) was substantially higher in the DM-GA-MLPCL group (80.60±2.07) compared to the SCI (8.80±1.48), DM-GA (70.40±3.74), and MM-PCL (7.00±1.41) groups. Conversely, GFAP intensity (glial scarring) was significantly lower in the DM-GA-MLPCL group (78.40±5.02) than in the SCI (226.80±1.92) and DM-GA (175.20±6.53) groups, and higher than the cavitated MM-PCL group (18.80±1.48).

In summary, the DM-GA-MLPCL scaffold robustly promoted key aspects of neural repair, including neuronal survival/regeneration, dendritic remodeling, and axonal growth across the lesion, while concurrently attenuating glial scar formation. Consequently, it facilitates the re-establishment of neural circuits across the injury site.

Furthermore, these findings indicate that SCI rat models treated with DM-GA-MLPCL are likely to exhibit significant improvements in motor and sensory functions.

2.11 Evaluation of motor function recovery

Motor functional recovery was assessed using the Basso, Beattie, and Bresnahan (BBB) locomotor rating scale for overall locomotion and the CatWalk XT system for detailed gait analysis to indicate functional restoration [42]. All rats had a preoperative BBB score of 21. By 28 days post-injury (dpi), the DM-GA-MLPCL group achieved a mean BBB score of 16, which was significantly greater than those of

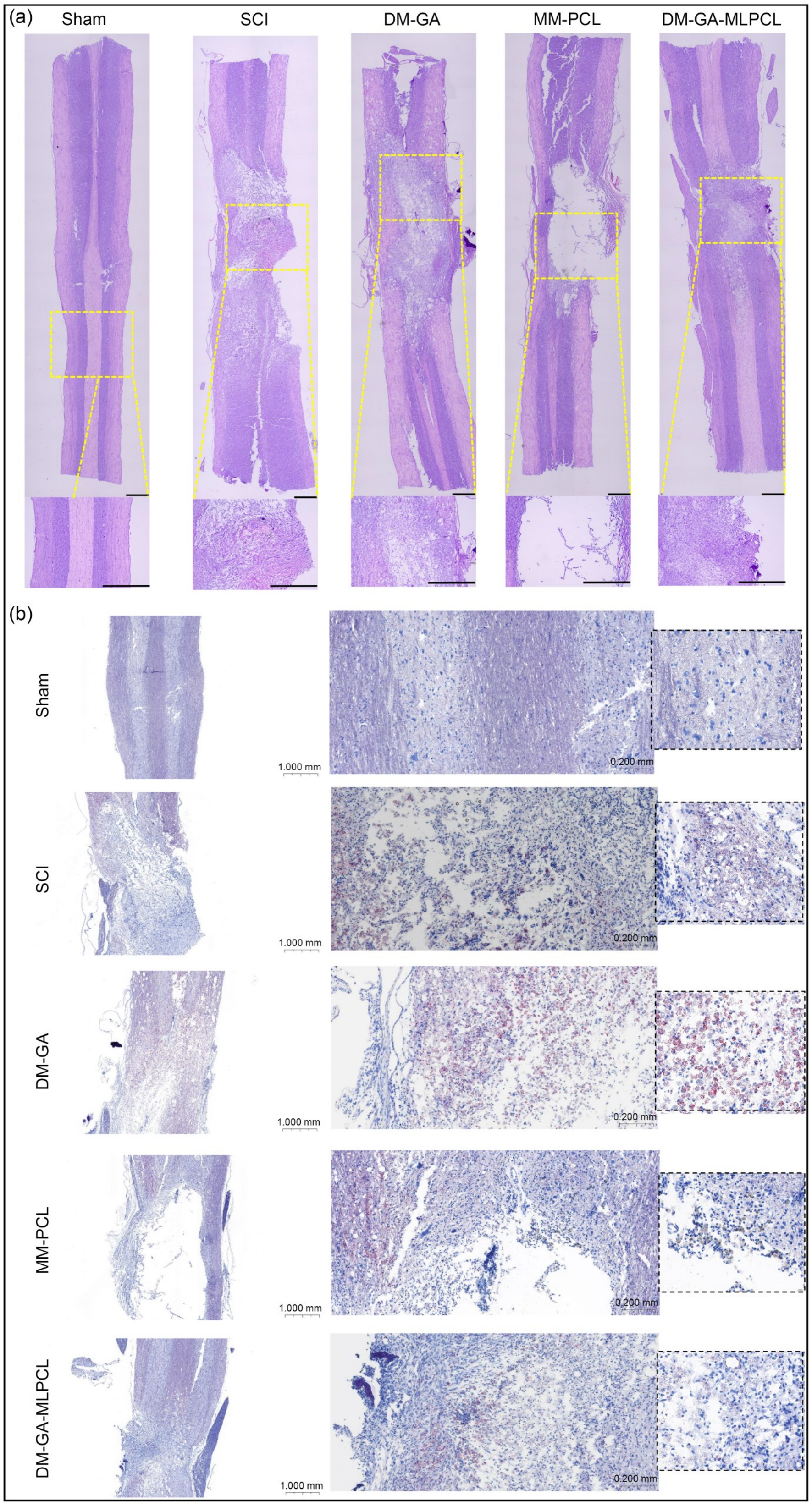

Fig. 6 Histological assessment of spinal cord recovery after SCI. Masson staining (a) and the corresponding ORO-stained images (b) of spinal cord samples from the sham, SCI, DM-GA, MM-PCL, and DM-GA-MLPCL groups at six weeks post-SCI. The scale bars for (a) and (b) are 200 μm (5×)/200 μm (10×) and 1 mm (5×)/200 μm (20×), respectively. The small inset on the right shows a magnified view of the local ORO red markers for easier observation of each sample group

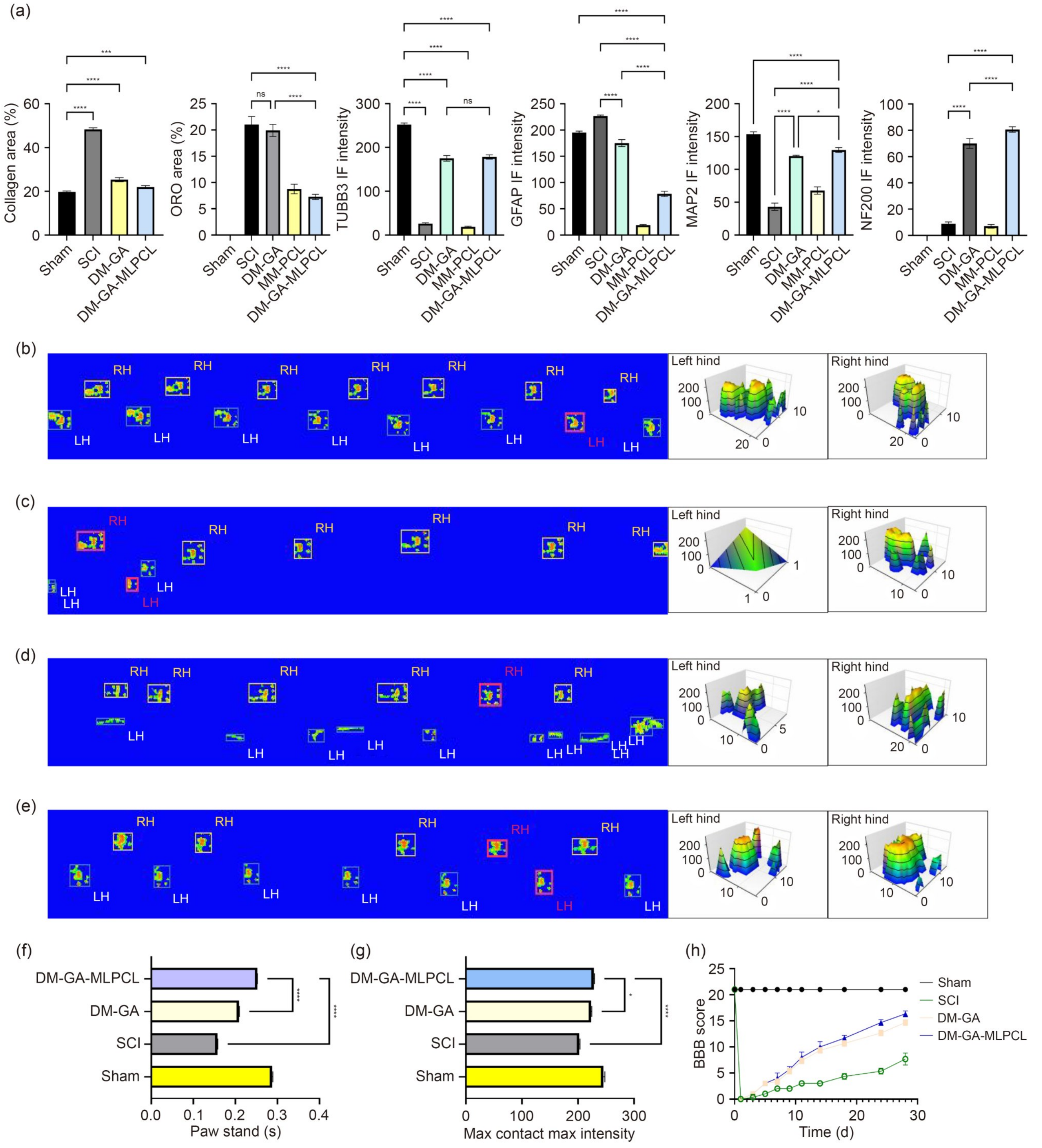

Fig. 7 Behavioral assessment of spinal cord recovery after SCI. (a) Summary of quantitative statistical results. From left to right: the area ratios of Masson-stained collagen and ORO staining (n=5 for both); the IF intensities of TUBB3, GFAP, MAP2, and NF200 (n=5 for all). Gait patterns of the sham (b), SCI (c), GA (d), and DM-GA (e) groups. Quantitative statistics of paw stand durations (f) and max contact max intensity (g) for Sprague–Dawley rats in the four groups (n=5). (h) BBB score statistics (n=5). Data in (a, f–h) are expressed as mean±standard deviation. ns: no significance; $^{*}p<0.05$, $^{***}p<0.001$, and $^{****}p<0.0001$

the SCI (7) and DM-GA (14) groups (Fig. 7h). A BBB score of 16 indicates consistent weight-supported plantar stepping, frequent forelimb-hindlimb coordination, and predominantly parallel paw position during locomotion, with only occasional dorsal stepping. CatWalk gait analysis revealed significant improvements in the DM-GA-MLPCL group. Specific parameters such as paw stand (duration of paw contact with the glass plate) and max contact max

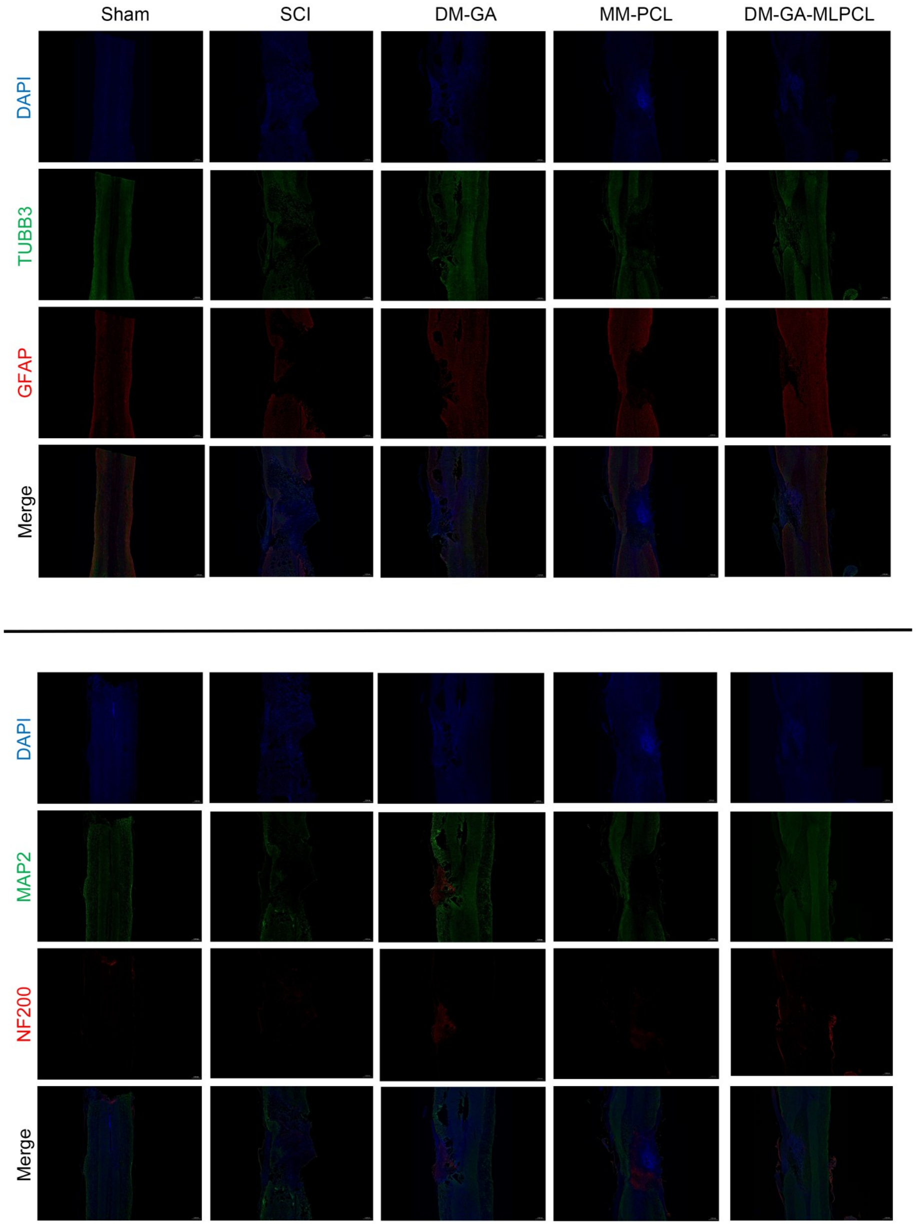

Fig. 8 IF staining images of TUBB3, GFAP, MAP2, and NF200 in spinal cord samples from the sham, SCI, DM-GA, MM-PCL, and DM-GA-MLPCL groups. Scale bars: 500 μm (2×)

intensity (peak pressure exerted during stance) were significantly greater in the DM-GA-MLPCL group compared to the SCI and DM-GA groups (Figs. 7b–7g), indicating improved weight-bearing capacity and locomotor function.

Together, the behavioral data demonstrate that DM-GA-MLPCL treatment significantly restored locomotor function, implicating improvements in spinal cord conduction, motor control, and neuromuscular performance.

2.12 Integrated omics analysis

To elucidate the molecular mechanisms by which DM-GA-MLPCL modulates lipid metabolism after SCI, we performed an integrated lipidomic and proteomic analysis on spinal cord tissues collected six weeks post-injury. A comparative study between the DM-GA-MLPCL and SCI groups was performed to identify key regulatory pathways and to validate the therapeutic mechanism of the composite scaffold.

Lipidomic profiling identified 2314 metabolites (n=4), of which phosphatidylcholine (PC) and phosphatidylethanolamine (PE) were the most abundant, consistent with the known lipid composition of the CNS and previous studies [43]. Orthogonal partial least squares-discriminant analysis (OPLS-DA) showed a clear separation between the DM-GA-MLPCL and SCI groups (Fig. 9a). Differential analysis revealed that several lipid species were significantly

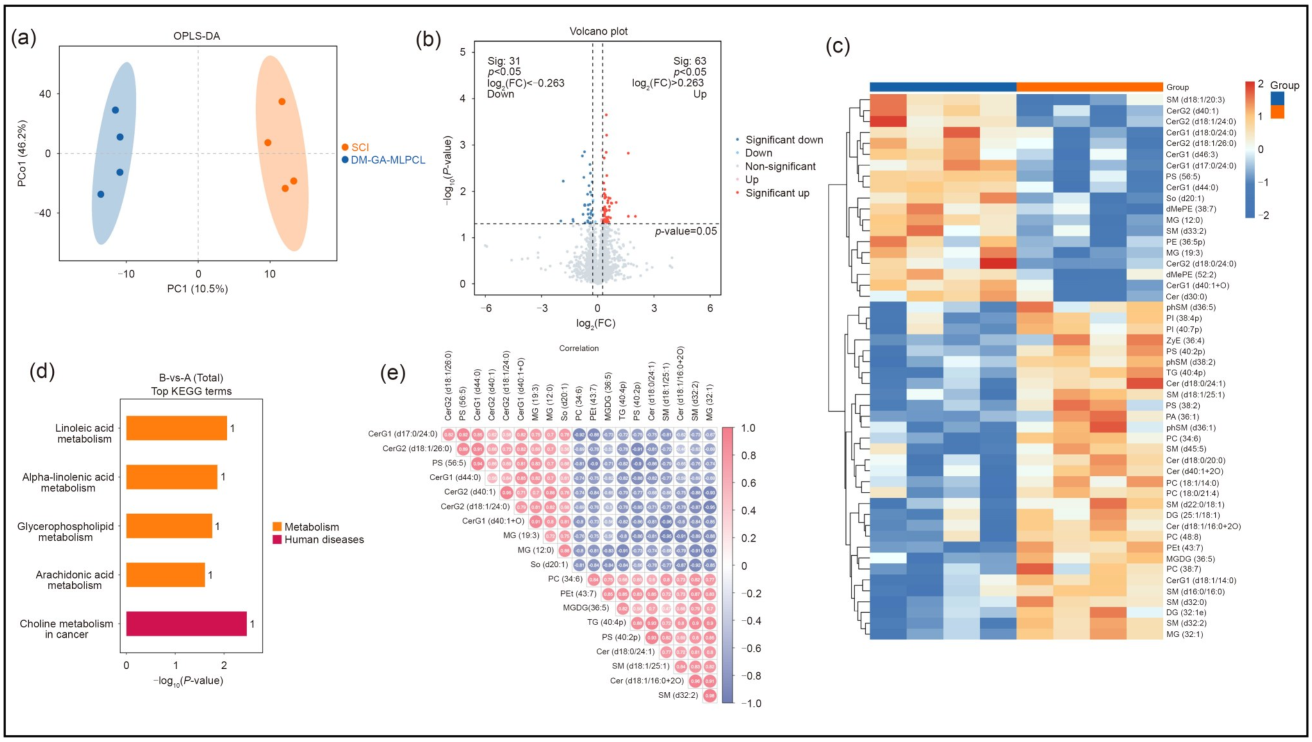

Fig. 9 Lipidomics analysis of spinal cord samples at six weeks post-SCI (n=4). (a) Orthogonal projections to latent structures discriminant analysis (OPLS-DA) comparing the SCI (orange) and DM-GA-MLPCL groups (blue). Volcano plot (b) and hierarchical clustering heatmap (c) of differential analysis (DM-GA-MLPCL and SCI groups are marked in blue and orange, respectively). (d) KEGG pathway enrichment analysis (Letters A and B indicate DM-GA-MLPCL and SCI groups, respectively). (e) Correlation analysis of metabolites

altered, with ceramide hexoside (CerG), PC, triglyceride (TG), PE, and monoacylglycerol (MG) being among the most prominently affected (Figs. 9b and 9c). Compared to the SCI group, in the DM-GA-MLPCL group, CerG2 (d40: 1), CerG2 (d18:1/24:0), and CerG1 (d18:0/24:0) were significantly upregulated, whereas TG (40:4p), PC (18:1/14:0), and PC (18:0/21:4) were downregulated.

Kyoto Encyclopedia of Genes and Genomes (KEGG) analysis (Fig. 9d) of differential metabolites revealed that the pathways enriched between the two groups mainly included unsaturated fatty acid metabolism and glycerophospholipid metabolism. CerG, a sphingolipid metabolic intermediate involved in glycosphingolipid synthesis, regulates cell proliferation and apoptosis. Elevated CerG levels often indicate lysosomal hyperfunction [44, 45]. Previously, TG was shown to be a critical metabolic site for foam cell formation. The dynamic balance between CerG and TG reflects the flux of lipid synthesis and degradation (Fig. 9e) [5].

In the proteomic analysis (n=4), significant differences were observed between the DM-GA-MLPCL and SCI groups (Figs. 10a–10c). During the pathway enrichment analysis of differential metabolites, Gene Ontology (GO) (Fig. 10d) and KEGG (Fig. 10e) analyses revealed that the metabolic pathways were primarily associated with nucleotide excision repair, RNA polymerization, protein kinase activity, and lysosomal function. In the differential protein–protein interaction (PPI) network analysis (Fig. 10f), P10247:Cd74 was predominantly involved in macrophage migration and the regulation of inflammation. G3V8Y5: Polr2b and E9PTR3:Drosha were mainly implicated in the post-transcriptional regulation of gene expression [46].

Comparison of the combined proteomic and lipidomic profiles of differential metabolites (Fig. 11a) indicated that CerG2 (d40:1) and TG (40: 4p) exhibited the most significant differences between the DM-GA-MLPCL and SCI groups, implicating substantial regulation of lipid synthesis and degradation. Additionally, TGs and PCs, which contain palmitic acid chains, were significantly downregulated in the DM-GA-MLPCL group. Figure 11b depicts the shared pathways of differentially expressed proteins and lipid metabolites, denoting enrichment in choline metabolism, diabetes-associated lipid synthesis, glycerophospholipid metabolism, and necroptosis.

In summary, integrated multi-omics analysis demonstrated that DM-GA-MLPCL induces substantial remodeling of the lipid metabolic landscape in SCI. The regulation of key lipid species, particularly TG and CerG, and the associated metabolic pathways provides a molecular basis for the therapeutic efficacy of the DM-GA-MLPCL biocomposite, establishing its mechanism of action.

3 Discussion

Building on previous knowledge, this work developed a dual-matrix acellular HAAM hydrogel integrated with a foam-cell MM-PCL nanofiber membrane for treating SCI. Both components were meticulously engineered and rigorously evaluated to confirm their biocompatibility and the absence of mutual functional interference.

The pathological cascade of SCI unfolds in distinct cellular phases. Microglia activation occurs within minutes, initiating the inflammatory response [47]. This is followed by a massive infiltration of neutrophils, which peaks around 3 dpi but subsides rapidly due to their short lifespan [48]. Concurrently, BMDMs begin infiltrating the lesion by approximately 3 dpi, becoming the dominant phagocytic population by 7 dpi due to their superior phagocytic capacity and sustained presence at the injury site [49]. However, the phagocytic activity of BMDMs becomes detrimental in the chronic phase. The persistent release of lipid-rich myelin debris over weeks post-SCI leads to lipid overload in BMDMs, disrupting their intracellular lipid homeostasis. This triggers their pathological transformation into foam cells, which are phenotypically similar to those found in atherosclerotic plaques [8]. These foam cells accumulate in the

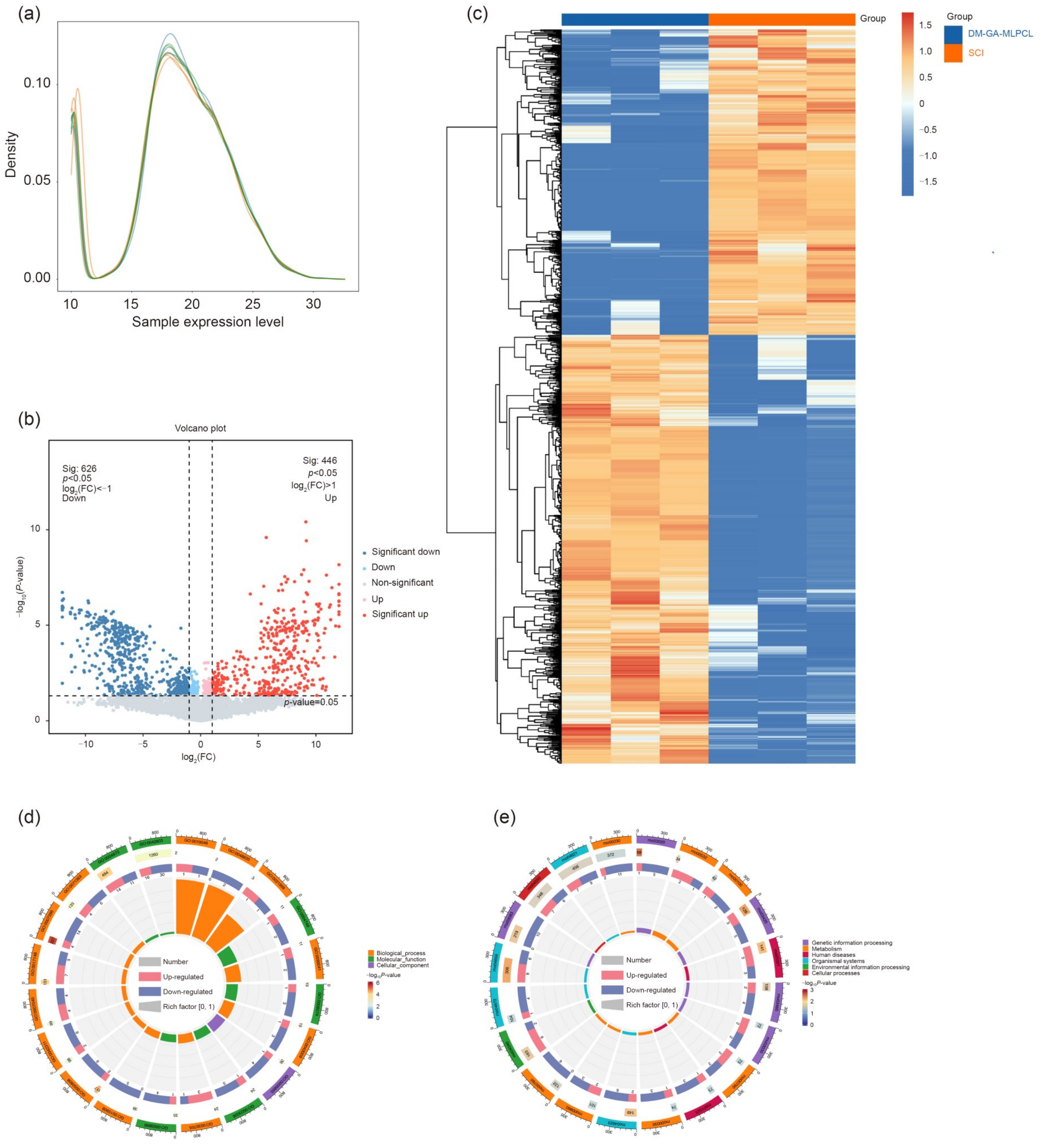

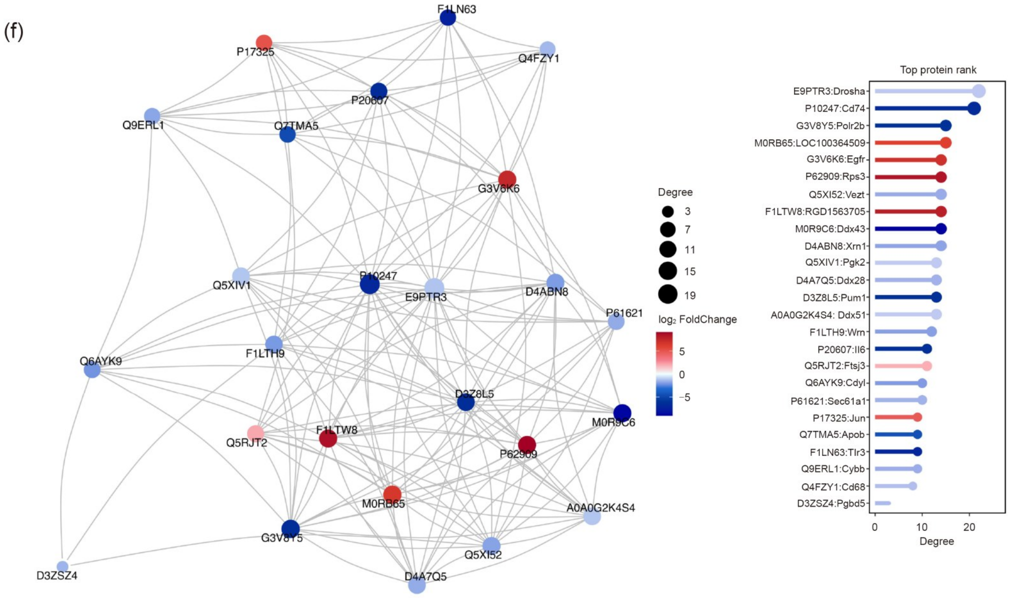

Fig. 10 Proteomic analysis of spinal cord samples at six weeks post-SCI (n=4). (a) Protein expression analysis curves of the samples. Volcano plot (b) and hierarchical clustering heatmap (c) of the differentially expressed proteins. GO (d) and KEGG (e) pathway enrichment analyses and their respective circos diagrams. (f) Differential PPI network analysis. FC: fold change

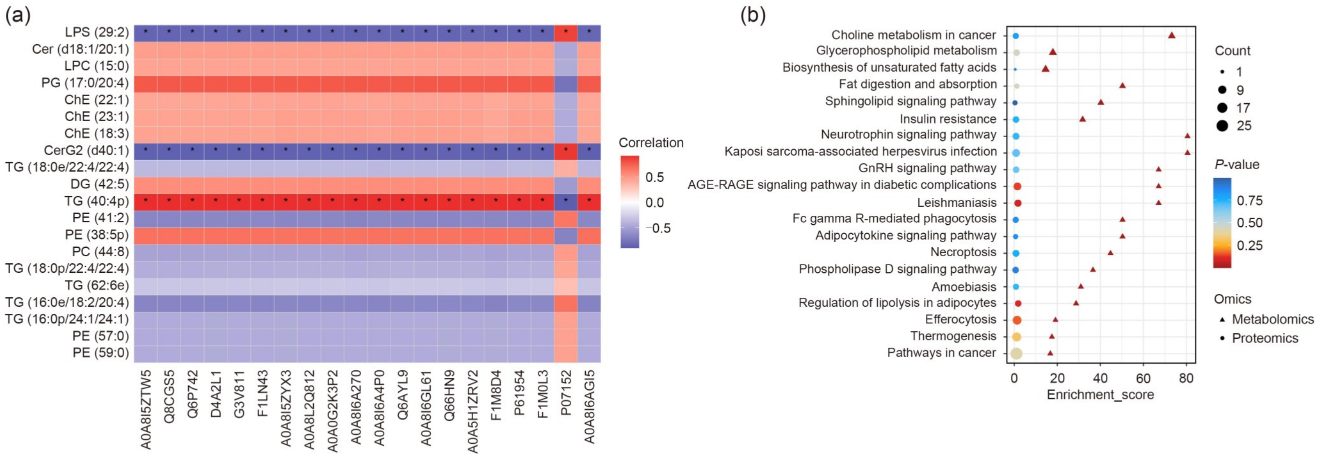

Fig. 11 Multi-omics analysis of metabolites and proteins (n=12). Correlation (a) and common pathway analyses (b) between differentially expressed metabolites and differentially expressed proteins

lesion core, where they drive inflammation, fibroblast proliferation, and fibrotic scar formation, impeding recovery [43].

There are three predominant perspectives for combating foam cells in SCI: first, reducing the adsorption of myelin debris by phagocytes [8, 9, 43]; second, enhancing the lipophagic capability of phagocytes themselves [10, 11]; third, promoting intracellular lipid efflux in the phagocytes [12]. These three approaches primarily focus on regulating cellular activities through therapeutic interventions. All of them can partially inhibit the transformation of BMDMs into foam cells, thereby facilitating recovery following SCI.

Here, we highlight that these approaches address the consequences (foam cell formation) rather than the root cause: the persistent spatial accumulation of myelin debris. As long as myelin debris remains abundant, BMDMs will continue phagocytosing until they become lipid-laden, sedentary foam cells that contribute to scar formation. The lipids in these cells have been shown to be predominantly derived from engulfed myelin, rather than de novo synthesis [5, 50]. Therefore, the extracellular burden of myelin debris is the primary driver of foam cell formation. Our strategy, using DM-GA-MLPCL to clear myelin debris from the lesion site actively, addresses this fundamental issue. By reducing the debris load, we mitigate its direct neurotoxicity, prevent foam cell accumulation, inhibit fibrotic scarring, and create an environment conducive to axonal regeneration.

The integration strategy for the DM-GA and MM-PCL components was carefully considered. We explored, but ultimately rejected, chemical grafting into a single entity to avoid potentially compromising their individual bioactivities. Instead, we adopted a spatially defined implantation strategy: DM-GA was placed in the lesion core to reconstruct gray matter, while MM-PCL was positioned in the surrounding white-matter tracts [51]. The two components play distinct yet complementary roles, timed to the pathophysiological cycle of SCI. The implantation of DM-GA hydrogel in the lesion core helps reconstruct gray matter architecture. It leverages the bioactive properties of HAAM to mitigate inflammation, promote angiogenesis, and provide a supportive microenvironment for axonal regeneration. The dual-matrix modification further enhances the recruitment and migratory capacity of BMDMs. With a degradation profile spanning the acute and subacute phases, DM-GA provides timely release of neurotrophic factors. Conversely, the MM-PCL membrane, positioned in the adjacent white matter, facilitates myelin debris clearance—a function not inherent to HAAM. Its long-lasting degradation ensures continuous removal of myelin debris and associated foam cells throughout the sub-acute and chronic phases, thereby effectively suppressing fibrotic scar deposition. This spatial and temporal division of labor underpins the therapeutic synergy of DM-GA-MLPCL.

The fabrication process was designed to be mild, avoiding harsh chemical crosslinkers, extreme temperatures, and irradiative steps to preserve the inherent biological functions of HAAM. Furthermore, as demonstrated by our in vitro assays, the composite scaffold does not hinder BMDM migration, a process critical to its mechanism of action and overall in vivo efficacy.

This work builds upon and refines our previous research [13, 14, 19] within a cohesive strategic framework for SCI repair. As discussed earlier, although the two components of DM-GA-MLPCL appear to function independently, they, in fact, play distinct therapeutic roles at different stages of SCI. The inclusion of an MM-PCL-only group in our histological assessment was critical for validating the composite strategy. The severe cavitation observed in this group illustrates the consequences of omitting the structural support and bioactive properties provided by the DM-GA hydrogel, leading to mechanical failure and disrupted tissue homeostasis. This finding strongly underscores the critical role of HAAM-based components beyond myelin debris clearance. Instead, it highlights the indispensable role of HAAM's rich neurotrophic and matrix components during acute-phase repair, underscoring the necessity of the combined DM-GA-MLPCL system.

Choosing an axially aligned PCL nanofiber membrane was a conscious decision. Among the architectures evaluated (e.g., random, porous sponge, concentric), aligned fibers were selected for their ability to mimic the topographic organization of the white matter's longitudinal axonal tracts. This alignment provides crucial contact guidance for regenerating axons, promoting directed elongation across the lesion while minimizing aberrant branching and potential maladaptive circuit formation [51]. This oriented structure also offers a versatile platform for future functionalization, such as the graded delivery of bioactive factors or integration with electroconductive components [52, 53].

To achieve a uniform, functional cell membrane coating on PCL nanofibers, we combined liposome extrusion with ultrasonic vibration, overcoming the limitations of traditional coating techniques. The extruder produces monodisperse membrane vesicles while preserving protein integrity, ensuring that the coating retains key macrophage biomarkers, which are crucial for its targeting and immunomodulatory functions [52, 54]. Concurrent ultrasonic treatment enhances vesicle adsorption and bonding to the fiber surface while preventing aggregation in solution, guaranteeing coating homogeneity [55]. This versatile coating strategy is readily adaptable for loading therapeutic agents or incorporating additional bioactive elements in the future.

Previous strategies addressing the myelin debris-foam cell issue primarily focused on modulating phagocytic activity via molecular interventions. In contrast, biomaterial-based approaches for this specific problem remain relatively unexplored. Here, we introduce a novel paradigm: a biomaterial scaffold with a functional foam-cell membrane coating that directly and continuously sequesters myelin debris within the lesion microenvironment. This "debris-sink" strategy tackles the problem at its source, circumventing potential side effects of cellular manipulation and leveraging the natural affinity of the foam cell membrane for its substrate. Our work leverages the unique ability of bioengineered materials to physically navigate the inhibitory CNS microenvironment, offering a distinct advantage for promoting neural regeneration.

Multi-omics analysis (lipidomics/proteomics) of spinal cord tissues at six weeks post-SCI provided critical mechanistic insights. Lipidomics identified several key lipid species altered by DM-GA-MLPCL treatment, including upregulation of CerG and downregulation of TG and specific PC. Notably, the reduction in TG aligns with the established role of TGs as core components of foam cell lipid droplets [5]. The downregulation of TG and PC reflects a reduction in the lipid burden in foam cells and, consequently, a decrease in their pro-inflammatory activity. In contrast, increased accumulation of CerG may promote neuronal survival by modulating sphingolipid signaling pathways. KEGG enrichment analysis indicated that the intervention primarily affected glycerophospholipid and unsaturated fatty acid metabolic pathways, which parallel lipid metabolic shifts reported in other foam cell pathologies.

While this study establishes a promising biomaterial-based strategy for myelin debris management in SCI, several limitations warrant attention in future work. First, fine-tuning the mechanical properties of DM-GA to better match the native spinal cord parenchyma could enhance integration and reduce mechanical mismatch. Second, optimizing the degradation profiles of both components to better align with the remyelination timeline would be beneficial. Lastly, the multi-omics data provide a roadmap for future refinement, suggesting potential targets to enhance the bioactivity of either the hydrogel or the membrane coating. Despite these areas for improvement, the significance of this work lies in the composite biomaterials that can effectively ameliorate myelin debris accumulation and foam cell-driven pathology, opening a new avenue for comprehensive SCI treatment. Further development of this platform holds promise for achieving greater neurological recovery.

4 Conclusions

In this study, we focused on transferring myelin debris to treat SCI and addressed the limitations of previously designed biocompatible materials. This work innovatively employed a foam cell membrane that can absorb myelin debris as the key improvement, leveraging the advantages of biomaterials over other mainstream treatment methods within a multidisciplinary context. We designed MM-PCL using a PCL nanofiber membrane as a carrier for the foam cell membrane coating. Simultaneously, DM-GA was fabricated using macrophage-derived ECM-modified HAAM to facilitate BMDM migration toward MM-PCL. We confirmed that the uptake ability of MM-PCL stemmed from the increased membrane receptors on the foam cell membrane, validated the capacity of DM-GA to promote BMDM migration, and tested the biocompatibility of DM-GA-MLPCL. In vitro and in vivo experiments demonstrated that DM-GA-MLPCL fully retains the bioactivity of HAAM, with its components exerting synergistic effects to promote spinal cord repair, reduce scar formation, and enhance motor function recovery. This work highlights the unique properties of biomaterials designed based on the myelin debris-transferring strategy for SCI, addressing the conflict between foam cells and myelin debris and providing novel insights into the entire pathological process and multi-targeted treatment of SCI.

Supplementary Information The online version contains supplementary material available at https://doi.org/10.1631/bdm.2500461.

Acknowledgements This work was supported by the National Natural Science Foundation of China (Nos. 82371383 and 32371400), the Medical Research Projects of the Health Commission of Jiangsu Province (No. K2023006), the Clinical Special Research Project of Nantong University (No. 2024JZ052), and the Key Research Project of School-Land Collaboration at Jiangsu Vocational College of Medicine (No. 202490401). All the authors appreciate the efforts of the Department of Obstetrics, Affiliated Hospital of Nantong University, for kindly providing the human amniotic membrane. All the authors appreciate the valuable guidance from Professors Yijun Fu and Chi Chen from the School of Textile and Clothing, Nantong University. The authors would like to express gratitude to E Ceshi for their support in providing the detection equipment used in this work. The authors would like to express gratitude to Keyan Zhinanzhen for their support in providing the detection technology used in this work.

Author contributions TX was responsible for the design of the experimental procedure, verified the composite material, participated in the whole process of experiments, and wrote the article. YCZ and XHN were responsible for the preparation and validation of the acellular amniotic membrane and the design of in vitro animal experiments. WH was responsible for photographing the in vitro cell experiments, verified the composite material, and wrote the article. MKL was responsible for data collection for the in vitro experiments. WS and RYH were responsible for all data integration and collating. YHZ was responsible for reviewing the correctness of the experimental design. YMY and XQC were responsible for reviewing the correctness of the experimental design, the rigor of the experimental verification, and the final review of the paper.

Declarations

Conflict of interest The authors declare that they have no conflict of interest.

Ethical approval All experimental procedures were performed in accordance with the Guide for the Care and Use of Laboratory Animals of the National Research Council. The animal ethics approval was approved by the Animal Care and Use Committee of Nantong University (Nantong, China; approval number: 22020214810).

Data availability Data will be made available on request. TX is responsible for receiving contact to provide relevant data.

Use of generative AI tools No generative AI tools were used in the preparation of this manuscript.

References

1. Zipser CM, Cragg JJ, Guest JD et al (2022) Cell-based and stem-cell-based treatments for spinal cord injury: evidence from clinical trials. *Lancet Neurol* 21(7):659–670. https://doi.org/10.1016/S1474-4422(21)00464-6
2. O'Shea TM, Burda JE, Sofroniew MV (2017) Cell biology of spinal cord injury and repair. *J Clin Investig* 127(9):3259–3270. https://doi.org/10.1172/jci90608
3. Pukos N, Marion CM, Arnold WD et al (2023) Chronic demyelination and myelin repair after spinal cord injury in mice: a potential link for glutamatergic axon activity. *Glia* 71(9): 2096–2116. https://doi.org/10.1002/glia.24382
4. Shuman SL, Bresnahan JC, Beattie MS (1997) Apoptosis of microglia and oligodendrocytes after spinal cord contusion in rats. *J Neurosci Res* 50(5):798–808. https://doi.org/10.1002/(SICI)1097-4547(19971201)50:5<798::AID-JNR16>3.0.CO;2-Y
5. Kloosterman DJ, Erbani J, Boon M et al (2024) Macrophage-mediated myelin recycling fuels brain cancer malignancy. *Cell* 187(19):5336–5356. https://doi.org/10.1016/j.cell.2024.07.030
6. Li DY, Yang KH, Li JL et al (2024) Single-cell sequencing

reveals glial cell involvement in development of neuropathic pain via myelin sheath lesion formation in the spinal cord. *J Neuroinflammation* 21(1):213. https://doi.org/10.1186/s12974-024-03207-3

7. Li JX, Zhu ZY, Li YT et al (2022) D-4F, an apolipoprotein A-I mimetic, promotes the clearance of myelin debris and the reduction of foamy macrophages after spinal cord injury. *Bioengineered* 13(5):11794–11809. https://doi.org/10.1080/21655979.2022.2073063
8. Wang X, Cao K, Sun X et al (2015) Macrophages in spinal cord injury: phenotypic and functional change from exposure to myelin debris. *Glia* 63(4):635–651. https://doi.org/10.1002/glia.22774
9. Zhu Y, Lyapichev K, Lee DH et al (2017) Macrophage transcriptional profile identifies lipid catabolic pathways that can be therapeutically targeted after spinal cord injury. *J Neurosci* 37(9):2362–2376. https://doi.org/10.1523/JNEUROSCI.2751-16.2017
10. Sergin I, Bhattacharya S, Emanuel R et al (2016) Inclusion bodies enriched for p62 and polyubiquitinated proteins in macrophages protect against atherosclerosis. *Sci Signal* 9(409):ra2. https://doi.org/10.1126/scisignal.aad5614
11. Razani B, Feng C, Coleman T et al (2012) Autophagy links inflammasomes to atherosclerotic progression. *Cell Metab* 15(4): 534–544. https://doi.org/10.1016/j.cmet.2012.02.011
12. Zhou QS, Xiang HK, Li A et al (2019) Activating adiponectin signaling with exogenous AdipoRon reduces myelin lipid accumulation and suppresses macrophage recruitment after spinal cord injury. *J Neurotrauma* 36(6):903–918. https://doi.org/10.1089/neu.2018.5783
13. Zhou YC, Xu T, Zhou YY et al (2024) A review focuses on a neglected and controversial component of SCI: myelin debris. *Front Immunol* 15:1436031. https://doi.org/10.3389/fimmu.2024.1436031
14. Zhou YC, Xu T, Zhou YY et al (2025) A myelin debris cleaner for spinal cord injury recovery: polycaprolactone/cell membrane assembled scaffolds. *Adv Sci* 12(36):e03269. https://doi.org/10.1002/advs.202503269
15. Wang MG, Yang S, Cao Z et al (2020) Application of acellular tissue matrix for enhancement of weak abdominal wall in animal model. *BioMed Res Int* 2020:3475289. https://doi.org/10.1155/2020/3475289
16. Wu MF, Yu Z, Matar DY et al (2023) Human amniotic membrane promotes angiogenesis in an oxidative stress chronic diabetic murine wound model. *Adv Wound Care* 12(6):301–315. https://doi.org/10.1089/wound.2022.0005
17. Wang H, Tang Q, Lu Y et al (2023) Berberine-loaded MSC-derived sEVs encapsulated in injectable GelMA hydrogel for spinal cord injury repair. *Int J Pharm* 643:123283. https://doi.org/10.1016/j.ijpharm.2023.123283
18. Yang CW, Xu T, Lu Y et al (2024) Quercetin-loaded human umbilical cord mesenchymal stem cell-derived sEVs for spinal cord injury recovery. *Neuroscience* 552:14–28. https://doi.org/10.1016/j.neuroscience.2024.05.028
19. Xu T, Yang CW, Lu Y et al (2024) Photocrosslinkable human amniotic membrane hydrogel for recovery from spinal cord injury. *Bio-Des Manuf* 7(6):1035–1052. https://doi.org/10.1007/s42242-024-00318-x
20. Zhang J, Liu ZM, Li YW et al (2020) FGF-2-induced human amniotic mesenchymal stem cells seeded on a human acellular amniotic membrane scaffold accelerated tendon-to-bone healing in a rabbit extra-articular model. *Stem Cells Int* 2020:4701476. https://doi.org/10.1155/2020/4701476
21. Jia ZL, Ma HL, Liu JQ et al (2023) Preparation and characterization of polylactic acid/nano hydroxyapatite/nano hydroxyapatite/human acellular amniotic membrane (PLA/nHAp/HAAM) hybrid scaffold for bone tissue defect repair. *Materials* 16(5):1937. https://doi.org/10.3390/ma16051937
22. Hu Z, Dai M, Chang Y et al (2024) Strategies for arterial graft optimization at the single-cell level. *Nat Cardiovasc Res* 3(5): 541–557. https://doi.org/10.1038/s44161-024-00464-6
23. Rowley AT, Nagalla RR, Wang SW et al (2019) Extracellular matrix-based strategies for immunomodulatory biomaterials engineering. *Adv Healthc Mater* 8(8):e1801578. https://doi.org/10.1002/adhm.201801578
24. Pan YX, Zheng ZG, Zhang XL et al (2024) Hybrid bioactive hydrogel promotes liver regeneration through the activation of Kupffer cells and ECM remodeling after partial hepatectomy. *Adv Healthc Mater* 13(17):e2303828. https://doi.org/10.1002/adhm.202303828
25. Hodges SD, Wahman DG, Haupert LM et al (2023) Non-steady-state Fickian diffusion models decrease the estimated gel layer diffusion coefficient uncertainty for diffusive gradients in thin-films passive samplers. *Environ Sci Technol* 57(26):9793–9801. https://doi.org/10.1021/acs.est.3c01861
26. Faleeva M, Ahmad S, Theofilatos K et al (2024) Sox9 accelerates vascular aging by regulating extracellular matrix composition and stiffness. *Circ Res* 134(3):307–324. https://doi.org/10.1161/CIRCRESAHA.123.323365
27. Li GL, Gao F, Yang DL et al (2024) ECM-mimicking composite hydrogel for accelerated vascularized bone regeneration. *Bioact Mater* 42:241–256. https://doi.org/10.1016/j.bioactmat.2024.08.035
28. Zhang Q, Chang CW, Qian CY et al (2021) Photo-crosslinkable amniotic membrane hydrogel for skin defect healing. *Acta Biomater* 125:197–207. https://doi.org/10.1016/j.actbio.2021.02.043
29. Lee JK, Zheng BH (2012) Role of myelin-associated inhibitors in axonal repair after spinal cord injury. *Exp Neurol* 235(1):33–42. https://doi.org/10.1016/j.expneurol.2011.05.001
30. Zamanifard M, Khorasani MT, Daliri M (2023) Hybrid electrospun polyhydroxybutyrate/gelatin/laminin/polyaniline scaffold for nerve tissue engineering application: preparation, characterization, and in vitro assay. *Int J Biol Macromol* 235:123738. https://doi.org/10.1016/j.ijbiomac.2023.123738
31. Liu JJ, Chen D, Zhu XQ et al (2022) Development of a decellularized human amniotic membrane-based electrospun vascular graft capable of rapid remodeling for small-diameter vascular applications. *Acta Biomater* 152:144–156. https://doi.org/10.1016/j.actbio.2022.09.009
32. Liu CJ, Liu DX, Zhang XC et al (2023) Nanofibrous polycaprolactone/amniotic membrane facilitates peripheral nerve regeneration by promoting macrophage polarization and regulating inflammatory microenvironment. *Int Immunopharmacol* 121: 110507. https://doi.org/10.1016/j.intimp.2023.110507
33. Liu K, Yan S, Liu Y et al (2024) Conductive and alignment-optimized porous fiber conduits with electrical stimulation for peripheral nerve regeneration. *Mater Today Bio* 26:101064. https://doi.org/10.1016/j.mtbio.2024.101064
34. Yao Z, Yuan WH, Xu JK et al (2022) Magnesium-encapsulated injectable hydrogel and 3D-engineered polycaprolactone conduit facilitate peripheral nerve regeneration. *Adv Sci* 9(21):2202102. https://doi.org/10.1002/advs.202202102
35. Golland B, Tipper JL, Hall RM et al (2022) A biomimetic nonwoven-reinforced hydrogel for spinal cord injury repair. *Polymers* 14(20):4376. https://doi.org/10.3390/polym14204376

36. Hu X, Xu W, Ren YL et al (2023) Spinal cord injury: molecular mechanisms and therapeutic interventions. *Signal Transduct Target Ther* 8(1):245. https://doi.org/10.1038/s41392-023-01477-6
37. Schaefer N, Andrade Mier MS, Sonnleitner D et al (2023) Rheological and biological impact of printable PCL-fibers as reinforcing fillers in cell-laden spider-silk bio-inks. *Small Methods* 7(10):e2201717. https://doi.org/10.1002/smtd.202201717
38. Ozcicek I, Aysit N, Balcikanli Z et al (2024) Development of BDNF/NGF/IKVAV peptide modified and gold nanoparticle conductive PCL/PLGA nerve guidance conduit for regeneration of the rat spinal cord injury. *Macromol Biosci* 24(5):e2300453. https://doi.org/10.1002/mabi.202300453
39. Liu ZN, Liu JJ, Liu N et al (2021) Tailoring electrospun mesh for a compliant remodeling in the repair of full-thickness abdominal wall defect - The role of decellularized human amniotic membrane and silk fibroin. *Mater Sci Eng C* 127:112235. https://doi.org/10.1016/j.msec.2021.112235
40. Kopper TJ, Gensel JC (2018) Myelin as an inflammatory mediator: myelin interactions with complement, macrophages, and microglia in spinal cord injury. *J Neurosci Res* 96(6):969–977. https://doi.org/10.1002/jnr.24114
41. Huang A, Huang Y, Yang WJ et al (2024) Fabrication of multifunctional silk nanofibril/hyaluronic acid scaffold for spinal cord repair. *Int J Biol Macromol* 263:130287. https://doi.org/10.1016/j.ijbiomac.2024.130287
42. Bhimani AD, Kheirkhah P, Arnone GD et al (2017) Functional gait analysis in a spinal contusion rat model. *Neurosci Biobehav Rev* 83:540–546. https://doi.org/10.1016/j.neubiorev.2017.09.007
43. Yao XQ, Chen JY, Garcia-Segura ME et al (2024) Integrated multi-omics analysis reveals molecular changes associated with chronic lipid accumulation following contusive spinal cord injury. *Exp Neurol* 380:114909. https://doi.org/10.1016/j.expneurol.2024.114909
44. Zadoorian A, Du XM, Yang HY (2023) Lipid droplet biogenesis and functions in health and disease. *Nat Rev Endocrinol* 19(8):443–459. https://doi.org/10.1038/s41574-023-00845-0
45. Zuo SM, Wang YX, Bao HJ et al (2024) Lipid synthesis, triggered by PPARγ T166 dephosphorylation, sustains reparative function of macrophages during tissue repair. *Nat Commun* 15(1):7269. https://doi.org/10.1038/s41467-024-51736-5
46. Liu LQ, Chen A, Li YX et al (2024) Spatiotemporal omics for biology and medicine. *Cell* 187(17):4488–4519. https://doi.org/10.1016/j.cell.2024.07.040
47. Davalos D, Grutzendler J, Yang G et al (2005) ATP mediates rapid microglial response to local brain injury in vivo. *Nat Neurosci* 8(6):752–758. https://doi.org/10.1038/nn1472
48. Fleming JC, Norenberg MD, Ramsay DA et al (2006) The cellular inflammatory response in human spinal cords after injury. *Brain* 129(12):3249–3269. https://doi.org/10.1093/brain/awl296
49. Kigerl KA, Gensel JC, Ankeny DP et al (2009) Identification of two distinct macrophage subsets with divergent effects causing either neurotoxicity or regeneration in the injured mouse spinal cord. *J Neurosci* 29(43):13435–13444. https://doi.org/10.1523/JNEUROSCI.3257-09.2009
50. Gao R, Song SJ, Tian MY et al (2024) Myelin debris phagocytosis in demyelinating disease. *Glia* 72(11):1934–1954. https://doi.org/10.1002/glia.24602
51. Han SF, Wang B, Jin W et al (2015) The linear-ordered collagen scaffold-BDNF complex significantly promotes functional recovery after completely transected spinal cord injury in canine. *Biomaterials* 41:89–96. https://doi.org/10.1016/j.biomaterials.2014.11.031
52. Guo HY, Wang XM, Wang KP et al (2025) Adsorption of natural organic matter and divalent cations onto/inside loose nanofiltration membranes: implications for drinking water treatment from rejection selectivity perspective. *Water Res* 282:123660. https://doi.org/10.1016/j.watres.2025.123660
53. He J, Qiao L, Li JH et al (2024) Advanced strategies for 3D-printed neural scaffolds: materials, structure, and nerve remodeling. *Bio-Des Manuf* 7(5):747–770. https://doi.org/10.1007/s42242-024-00291-5
54. Guo R, Li ZL, Shi JH et al (2025) Hyaluronic acid coating of poly(β-amino ester)/mRNA polyplexes enables ultra-high transfection efficiency. *J Control Release* 378:428–437. https://doi.org/10.1016/j.jconrel.2024.12.038
55. Wu JY, Huang H, Xu WJ et al (2026) Inflammation-driven biomimetic nano-polyphenol drug delivery system alleviates severe acute pancreatitis by inhibiting macrophage PANoptosis and pancreatic enzymes oversecretion. *J Adv Res* 79:783–799. https://doi.org/10.1016/j.jare.2025.04.006